Weakly Forced Mock Walker Cells

ZHIMING KUANG

Department of Earth and Planetary Sciences, and School of Engineering and Applied Sciences, Harvard University, Cambridge, Massachusetts

(Manuscript received 16 November 2011, in final form 20 April 2012)

ABSTRACT

Mock Walker cells driven by weak sea surface temperature (SST) forcing are studied using planetary-scale cloud system–resolving simulations and a simplified framework that represents convection with its linear response functions and parameterizes the large-scale flow based on the gravity wave equation. For sinusoidal SST forcings of the same amplitude, as the horizontal domain size increases, the mock Walker cells strengthen substantially and shorter vertical scales in the vertical velocity profile diminish. This is explained by the fact that temperature anomalies required to sustain a vertical velocity profile of given amplitude are stronger in cases of larger horizontal and smaller vertical scales. Such temperature anomalies become significant at planetary scales so that properly accounting for the horizontal momentum balance, including convective momentum transport (CMT), becomes necessary, while a weak temperature gradient approach that neglects horizontal momentum balance is no longer adequate. The downward advection component of the CMT in particular is important for capturing a number of features of the mock Walker cells. The extent of convective organization also affects the mock Walker cell through its effects on the sensitivities of convective heating and moistening to temperature and moisture anomalies. For strongly organized convection with deep inflows, these sensitivities are consistent with a layer mode of convective overturning, instead of the parcel mode as in unorganized convection, resulting in a weaker second baroclinic component in the mock Walker cells.

1. Introduction

Among the most basic behaviors of a moist convecting atmosphere is its response to a steady forcing, an extensively studied example being the determination of the tropical mean circulation for a given sea surface temperature (SST) distribution. However, our incomplete understanding of moist convection and imperfect parameterization of its effect in large-scale models have limited our ability to answer such questions, both theoretically and with global climate models. In this paper, we address a basic example of steady tropical circulations, namely mock Walker cells placed on the equator and driven by prescribed sinusoidal SST distributions in the longitudinal direction. We shall limit ourselves to SST forcings that are sufficiently weak so that the resulting circulations can be considered as linear perturbations upon a radiative–convective equilibrium (RCE) mean state. A good understanding of this basic, and linear, problem serves as a stepping stone toward understanding more nonlinear mock Walker cells that have deep convection concentrated over the warm SST and completely suppressed over the cold SST, as well as Walker and Hadley cells that include effects of Earth's rotation. Hereafter, we shall refer to mock Walker cells simply as Walker cells.

We will use a cloud system–resolving model (CSRM) with an elongated, planetary-scale, horizontal dimension, along which SST variations are prescribed, to explicitly simulate both the large-scale Walker cell and the small-scale convective processes. Notwithstanding issues such as inadequate resolution and uncertainties in parameterizing microphysics and subgrid-scale turbulence, contemporary CSRMs can credibly simulate many aspects of deep convective systems, and they represent a major step forward in realism compared to models with parameterized convection. As we shall describe, while weakly forced Walker circulations are among the simplest examples of steady tropical circulations, the CSRM simulations yield a number of results that are at first sight

Corresponding author address: Zhiming Kuang, Department of Earth and Planetary Sciences, and School of Engineering and Applied Sciences, Harvard University, 20 Oxford St., Cambridge, MA 02138.
E-mail: kuang@fas.harvard.edu

DOI: 10.1175/JAS-D-11-0307.1

counterintuitive. To better understand the behaviors of this system, we shall develop a simplified representation. We shall view the Walker cell as composed of many cumulus ensembles interacting with a large-scale circulation: the large-scale circulation affects the cumulus ensembles through vertical advections of temperature and moisture,[1] and the cumulus ensembles in turn change the (virtual) temperature profile and hence the horizontal pressure gradient that drives the large-scale circulation against momentum drag, the drag itself being effected by the cumulus ensembles as well. In a weakly forced Walker cell, because variations across the domain follow a single sinusoid, the interaction between a single instance of the cumulus ensemble (represented in a limited-area domain) and the large-scale circulation is sufficient to capture the behaviors of the system. We then make the following two simplifications.

The first is to represent the behavior of the cumulus ensemble with its linear response functions, as in Kuang (2010). Although cumulus convection involves nondifferentiable processes (variations of air parcel buoyancy across the water saturation point being one example), the statistics of a cumulus ensemble are expected to vary smoothly with its large-scale environment so that variations in the collective effect of the cumulus ensemble near a reference state may be approximated with a linear response function matrix. Define a state vector to include vertical profiles of temperature T, specific humidity q, and horizontal winds u, v, averaged horizontally over the limited area domain occupied by the cumulus ensemble. The linear response function matrix is a matrix $\mathbf{G}$ that, given the anomalous state vector (relative to a reference state vector), gives the anomalous convective tendencies as

$$\frac{d\mathbf{x}}{dt} = \mathbf{G}\mathbf{x}. \tag{1}$$

Equation (1) assumes that the domain-averaged state vectors (temperature, moisture, horizontal wind profiles) completely describe the statistical state of the limited area domain; that is, statistics of the cumulus ensemble are unique functions of the domain-averaged temperature, moisture, and horizontal wind profiles (Kuang 2010), an assumption well justified in the current steady-state problem.

While Kuang (2010) noted that the state vector could include the horizontal winds, that study limited the state vector to temperature and moisture. For the Walker cell problem, as we shall see, convective momentum transport (CMT) plays a key role. We shall therefore construct and present the linear response functions for temperature, moisture, and horizontal winds. As advocated in Kuang (2010), these linear response functions can be directly compared to those from convective schemes as a way of evaluating and improving such schemes.

As a second simplification, we parameterize the large-scale circulation in a simple form. More specifically, we use the state of a limited-area domain to compute the large-scale vertical motion in accordance with large-scale dynamics, and apply the advective tendencies associated with this vertical motion to convection in the limited area domain to represent feedbacks from the large-scale flow. This is a convenient strategy, both computationally and conceptually, to study large-scale circulations in a moist convecting atmosphere, and it has been used to study convectively coupled waves, tropical intraseasonal variability, tropical mean circulation, and cloud feedbacks (e.g., Sobel and Bretherton 2000; Bergman and Sardeshmukh 2004; Mapes 2004; Shaevitz and Sobel 2004; Raymond and Zeng 2005; Raymond 2007; Sobel et al. 2007; Kuang 2008; Blossey et al. 2009; Sessions et al. 2010; Kuang 2011).

Broadly speaking, in the context of tropical dynamics, there are two approaches often used to parameterize the large-scale vertical motion.

The first approach, known as the weak temperature gradient (WTG) approximation, recognizes the tendency for gravity waves to reduce the horizontal buoyancy gradient in the tropics and takes the large-scale vertical motion to be what is required to relax the horizontally averaged temperature profile in the limited-domain model back to a reference temperature profile (e.g., the tropical mean profile) over some time scale. The relaxation can be instantaneous so that temperature is fixed to the reference profile, or slower to allow deviations. While the tendency for small horizontal density gradients in the tropics has long been recognized (e.g., Charney 1963; Held and Hou 1980; Pierrehumbert 1995), exploiting this for use in limited-domain models was pioneered by Sobel and Bretherton (2000). This will be referred to as the relaxation or WTG approach and has been used in various forms in a number of studies (e.g., Sobel and Bretherton 2000; Shaevitz and Sobel 2004; Raymond and Zeng 2005; Raymond 2007; Sobel et al. 2007; Sessions et al. 2010; Wang and Sobel 2011).

The second approach, which we will refer to as the gravity wave approach, computes the vertical velocity based on two-dimensional (2D) gravity wave equations of a single horizontal wavenumber (Brown and Bretherton 1995; Caldwell and Bretherton 2009; Kuang 2008; Blossey et al. 2009; Kuang 2011). The approach of Kuang (2008), followed by Blossey et al. (2009) and Kuang (2011),

[1] In weakly forced Walker cells, horizontal advection of temperature and moisture can be neglected.

in particular, is suitable for use in CSRMs. In those studies, a Rayleigh momentum damping was used in the gravity wave equation. In this study, we will use the linear response functions of momentum that we derive from the CSRM and also a number of idealized forms of CMT.

There is indication that the relaxation and the gravity wave approaches may not give consistent results. For example, using the gravity wave approach, Kuang (2011) found that the shape of the large-scale vertical velocity profile and the closely related precipitation responses to a given surface heat flux forcing depend strongly on the coupling strength between convection and the large-scale flow [represented by the varying domain size in Kuang (2011)], while using their form of the relaxation approach, Wang and Sobel (2011) found a much weaker dependence. Therefore, as a second goal of this paper, we will use the weakly forced Walker cells as a test problem and compare results with parameterized large-scale dynamics against experiments in which the large-scale adjustment processes are explicitly simulated.

Through the above two simplifications, namely representing the cumulus ensemble with its linear response functions and parameterizing the large-scale flow, the weakly forced Walker cell problem will be reduced to a linear matrix problem, allowing better understanding of its behavior.

The paper is structured as follows. After a brief description of the CSRM used (section 2), we describe setups of the Walker cell experiments and present the simulations results (section 3). We then describe the linear response functions (section 4) and the approaches to parameterize feedbacks from the large-scale flow (section 5). The behaviors of the system when the linear response functions are coupled to the parameterized large-scale flow are presented and compared to the explicitly simulated Walker cells in section 6. We then offer our interpretations of the main behaviors observed in the system, examining the dependence on convective organization in section 7 and the role of CMT in section 8, before concluding in section 9.

2. Model description

All cloud system–resolving experiments are performed with the System for Atmospheric Modeling (SAM) version 6.8.2. SAM solves the anelastic equations of motion (Khairoutdinov and Randall 2003), with the prognostic thermodynamic variables of liquid water static energy, total nonprecipitating water, and total precipitating water. We use a bulk microphysics scheme, and a 1.5-order closure scheme for the effect of subgrid-scale turbulence. All experiments use the simple treatment of radiation of Pauluis and Garner (2006), where radiative cooling is set to -1.5 K day^{-1} in regions warmer than 207.5 K while a 5-day damping toward 200 K is used everywhere else.

All experiments are over an ocean surface with doubly periodic lateral boundary conditions. For simplicity, the surface latent and sensible heat fluxes are computed using bulk aerodynamic formula with a constant 10-m exchange coefficient of 1×10^{-3} and a constant surface wind speed of 5 m s^{-1} to eliminate any wind-induced surface heat exchange (WISHE) effect. Effects of WISHE will be explored in the future. Surface momentum fluxes are computed with the Monin–Obukhov similarity theory. Unless otherwise specified, the horizontal resolution is 2 km and there are 64 stretched vertical grid points that extend from the surface to 32 km, the top third of the domain being a wave-absorbing layer. The vertical grid size varies from 75 m near the surface to 500 m in the middle and upper troposphere.

3. Walker cell experiments

For the Walker cell experiments, the SST takes a sinusoidal form

$$\mathrm{SST}(x) = \mathrm{SST}_0 - \Delta\mathrm{SST}\cos\frac{2\pi x}{A}, \tag{2}$$

where A is the length of the long horizontal (or x) dimension, SST_0 is 28°C, and $\Delta\mathrm{SST} = 0.25°$ or 0.5°C, depending on the experiment. We ran simulations with five different domain sizes, with A = 16 000, 20 000, 25 000, 31 000, and 37 000 km, while keeping the short horizontal dimension at 64 km (32 grid points). The long x domain sizes were chosen to emphasize planetary-scale phenomena, with half domain sizes (containing a single overturning cell) of the longest domains comparable to that of the Walker cell over the Pacific Ocean. The short horizontal dimension is included to allow for more three-dimensional (3D) simulations of cloud-scale motions. We ran the 16 000-km case with a ΔSST of 0.5°C, the 31 000- and 37 000-km cases with a ΔSST of 0.25°C, and the 20 000- and 25 000-km cases with both ΔSST values. The ΔSST values were chosen for each case to produce a sizable signal while staying in the linear regime; as we shall show soon, the longer domain cases have substantially stronger responses to a given ΔSST. The 20 000- and 25 000-km cases were run with both ΔSST values to assess the sensitivity to the amplitude of the SST forcing. In all cases, the horizontal winds averaged horizontally across the domain were nudged to zero over a time scale of 1 h. The experiments were run for 200 days except the 37 000-km case, which was run for 150 days as the signal is already clear with this shorter integration

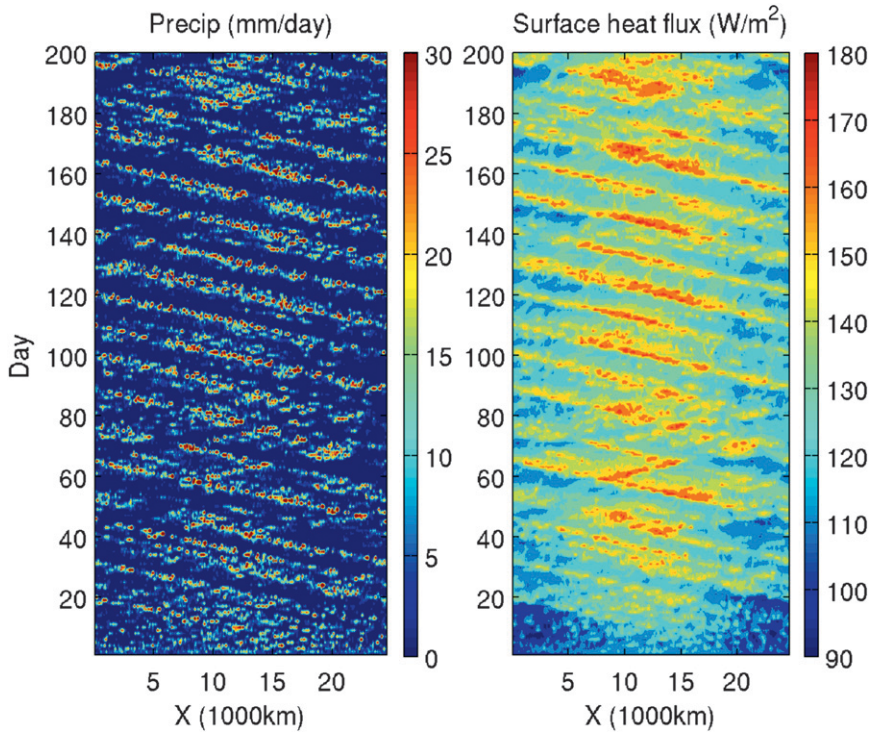

FIG. 1. (a) Precipitation and (b) total surface heat (sensible + latent) flux averaged over the short (y) dimension and plotted as a function of the long (x) dimension and time, for the 25 000 km × 64 km domain case.

time. The first 50 days of all simulations were considered the spinup period and excluded from time averages that we shall present.

While we have included the 64-km-wide y dimension to allow 3D convective motions, it is admittedly short and convection could still be artificially constrained to be more or less 2D. We have performed additional experiments with a y dimension of 1024 km. Three cases were performed with x-domain sizes of 16 000, 20 000, and 25 000 km, and with a 4-km horizontal resolution to reduce the computational cost. A ΔSST of 0.25°C was used for the 20 000- and 25 000-km cases, while a ΔSST of 0.5°C was used for the 16 000-km case to enhance the signal. These wider domain simulations were run for 125 days and the last 75 days were averaged to produce time averages.

We provide a general impression on the simulated Walker cells in Fig. 1, which shows, as a representative example, the simulated daily mean precipitation and surface heat fluxes (sensible plus latent) as a function of the long (x) dimension and time for the 25 000 km × 64 km domain case. Throughout this section, the variables that we present are averaged over the short (y) dimension. There are abundant convectively coupled waves in the domain and the surface heat fluxes are enhanced over the warm SST at the center of the domain. The stronger westward propagation arises by chance; in some other experiments, eastward-propagating waves are favored. Figure 2 shows the structure of the convective systems composited over a 50-day period. We shift 12-h averaged time slices in the x dimension so that the positions of their 500-hPa vertical velocity maximum are aligned and then average them together to make the composites. The horizontal velocities shown are Earth-relative. For system-relative velocities, one needs to add 14 m s^{-1} to account for the westward propagation. The composite structure, mostly associated with convectively coupled waves, shows strong organization with deep inflows that extend from the surface to about 400 hPa. Such deep inflows bear resemblance to observations of western Pacific mesoscale convective systems (Kingsmill and Houze 1999) and also the analytic model of slantwise layer overturning (Moncrieff 1992).

An example of the time-mean horizontal wind and perturbation pressure as a function of x and pressure is shown in Figs. 3a and 3b for the 25 000 km × 64 km case. Note that the surface pressure is higher over the warmer SST. The general patterns are very similar in the 25 000 km × 1024 km case, shown in Figs. 3c and 3d.

Figures 4 and 5 show the time-mean precipitation and total surface heat fluxes (thin lines), respectively, as well

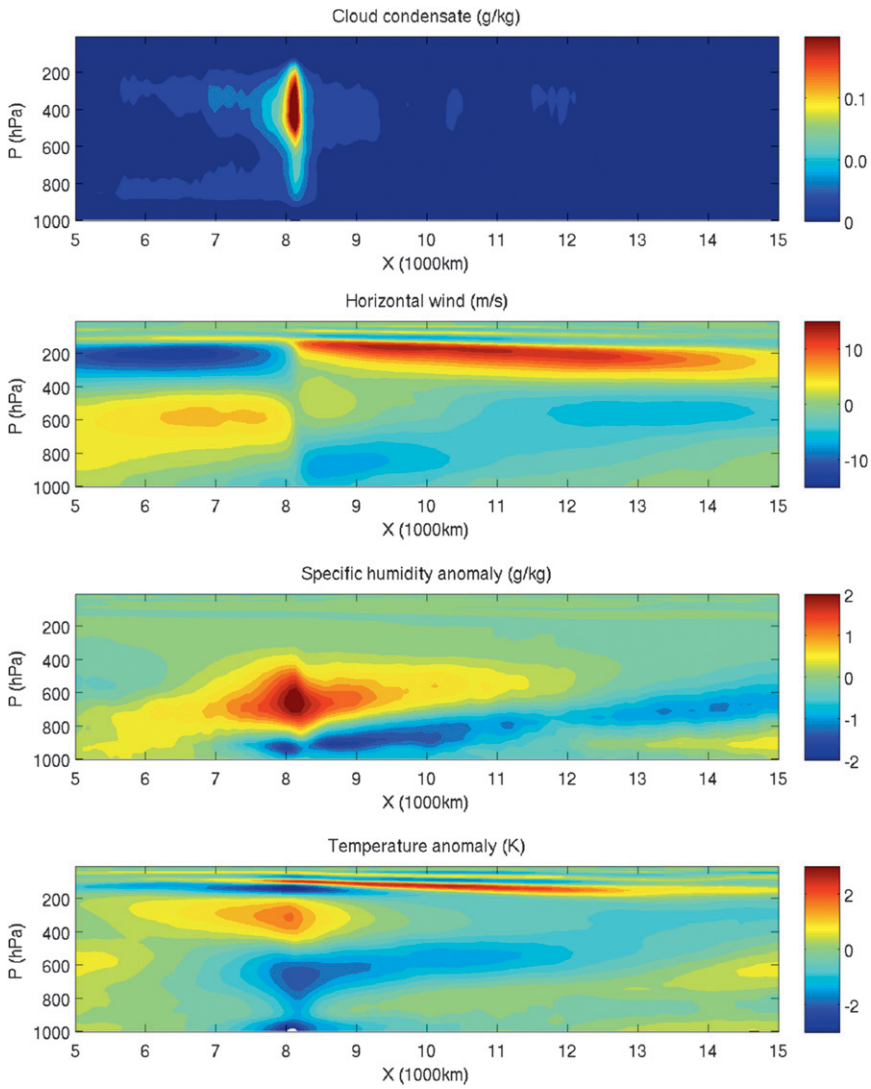

FIG. 2. Composite structures of the convective systems in the Walker simulations: (a) cloud condensates, (b) horizontal wind (Earth-relative), (c) specific humidity anomaly, and (d) temperature anomaly. The fields are averaged over the y dimension and composited over a 50-day period.

as the sums of their zeroth and first Fourier components (thick lines) as a function of the normalized x for the cases with a 64-km y dimension and various sizes in x. For all cases, including the 1024-km y-dimension cases not shown here, variations in surface heat fluxes are excellently described by their first Fourier components, and precipitation variations, while noisier, are also dominated by the first Fourier component, indicating a linear behavior, as SST variations contain only the first Fourier component. There is a slight phase shift in the 31 000-km case relative to the SST forcing. Since the surface heat fluxes are computed using the bulk formula with constant wind speed and exchange coefficients, the shift in the surface heat flux maximum results from anomalies in the surface air humidity and temperature. While this is the only case that shows this behavior, it is noteworthy that the system can sustain a surface heat flux maximum shifted away from the SST maximum.

Figure 6 summarizes the precipitation and surface heat flux responses in the different cases by showing the amplitudes of their first Fourier components. To provide some estimates of the uncertainties, for each case, we divide the period between day 50 and day 200 (day 150 in the 37 000-km case and day 125 in the wide y-dimension cases) into six subintervals of equal length, and compute the first Fourier components for time averages over the subintervals. We then divide the standard deviations among the six subintervals by $\sqrt{6}$ and plot them as the

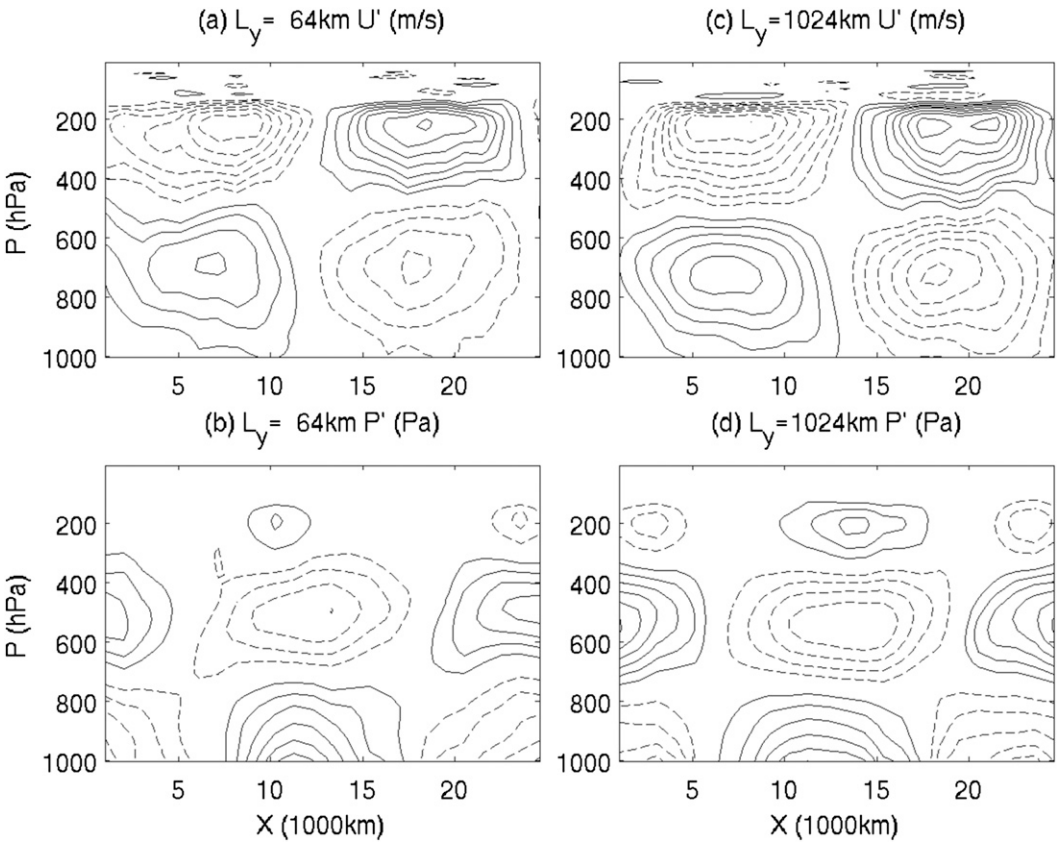

FIG. 3. Time-mean (a),(c) u winds and (b),(d) perturbation pressure averaged over the y dimension and plotted as a function of x and pressure, for experiments with (a),(b) a 25 000 km × 64 km horizontal domain and a horizontal resolution of 2 km and (c),(d) a 25 000 km × 1024 km horizontal domain size and a horizontal resolution of 4 km. The contour intervals are 0.5 m s^{-1} for u and 5 Pa for perturbations pressure. Positive contours are solid, negative contours are dashed, and zero contours are omitted.

estimated error bars. The tendency of stronger surface flux responses and even stronger precipitation responses at longer wavelengths is apparent. For the 20 000- and 25 000-km cases, the results with ΔSST values of 0.5° and 0.25°C are consistent within their uncertainties, indicating weak sensitivity to forcing amplitude and thus a linear behavior.

The slopes defined by the origin and the points in Fig. 6 are the reciprocals of the normalized gross moist stability (GMS), introduced by Neelin and Held (1987) and defined here as

$$\left\langle \omega \frac{\partial h}{\partial p} \right\rangle \Big/ \left\langle \omega \frac{\partial s}{\partial p} \right\rangle, \tag{3}$$

where ω is pressure velocity, s is the dry static energy, h is the moist static energy, and the angle brackets denote the mass-weighted vertical integral. In the present steady-state case, the numerator in Eq. (3) is balanced by surface heat fluxes (since radiation is fixed and horizontal advection is small) and the denominator is balanced by precipitation (since surface sensible heat flux is small), so that the normalized GMS is approximately the total surface heat fluxes divided by precipitation. Figure 6 shows that the normalized GMS decreases from 0.5 at 16 000 km to about 0.2 at 37 000 km. This change is almost entirely due to changes in the shape of the vertical velocity profiles, which will be described below.

The vertical profiles of pressure velocity, and normalized pressure velocity, temperature, specific humidity, u velocity, and perturbation pressure are shown in Fig. 7 for the 64-km y-dimension cases. The normalized profiles are calculated by dividing the profiles by the peak pressure velocities of their corresponding cases. Results for the 1024-km y-dimension cases are similar and thus omitted. To make these profiles, we filter each variable to retain only the first Fourier component in x and then take the profiles at the center of the domain, which has the warmest SST, for all fields except the u velocity, for which the profile at a quarter length of the

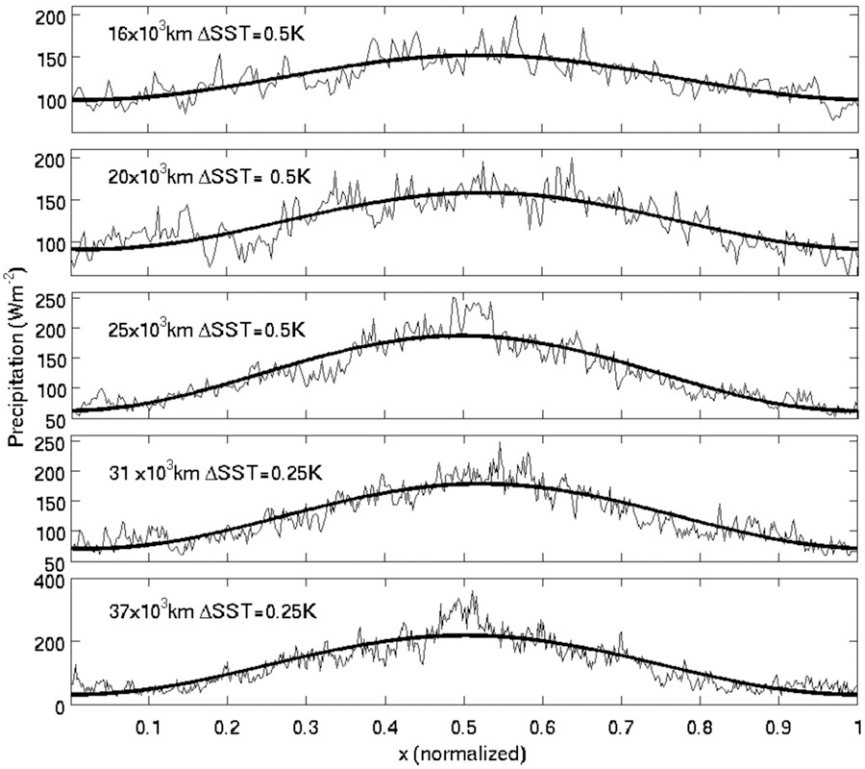

FIG. 4. Time-mean precipitation (thin lines) as a function of the normalized x coordinate for selected short y dimension (64 km) cases. The x dimension sizes (increasing from the top to the bottom) and the ΔSST used are labeled. The thick lines are the sum of the mean and the first Fourier component.

domain ($x = A/4$) is used. There are a number of notable features besides the stronger responses with the longer domain sizes. The vertical velocity profiles become progressively less top-heavy and have less of a second baroclinic vertical structure as the x-domain size increases; however, for the longer domain sizes, the temperature anomalies are dominated by a second baroclinic structure, being negative below about 500 hPa and positive above over the warmest SSTs, and the negative anomalies are stronger than the positive anomalies. As the x-domain size increases, this second baroclinic temperature anomaly slightly increases even though the second baroclinic structure in vertical velocity diminishes. Over the warmer SSTs, air is drier near the surface and moister aloft and becomes more so (after normalized by the peak pressure velocity) as the x-domain size increases. While near surface horizontal winds are convergent over the warmer SST, near-surface pressure is higher in all cases except in the 16 000-km case, where the surface pressure anomaly is close to zero. These features are consistent between the 64-km y-dimension and the 1024-km y-dimension simulations. Using pressure velocity profiles from Fig. 7 and the domain mean profiles of moist and dry static energy in Eq. (3), it is confirmed that the increase in the normalized GMS with domain size seen in Fig. 6 is due to the progressively less-top-heavy vertical velocity profiles.

As precipitation increases, surface air becomes colder and drier (Fig. 7) so that surface heat flux also increases. Because of the bulk formula used here, the precipitation–surface heat flux data in Fig. 6 roughly follow a line that intercepts the x axis at about 5 W m^{-2}, which is the surface heat flux variation due entirely to the SST (i.e., no surface air temperature and moisture variations; Fig. 6). Solution for each horizontal domain size is found along this line with a particular GMS.

We have also performed simulations for smaller domain sizes. However, as the domain size decreases, a resonance effect, also noted in Bretherton et al. (2006), starts to become apparent, which limits our investigation to the relatively long domain sizes discussed in this section.

The above, sometimes counterintuitive, results from this simple weakly forced Walker cell problem challenge our understanding of steady tropical flows. In the following two sections, we describe the two simplifications that we make to better understand this system.

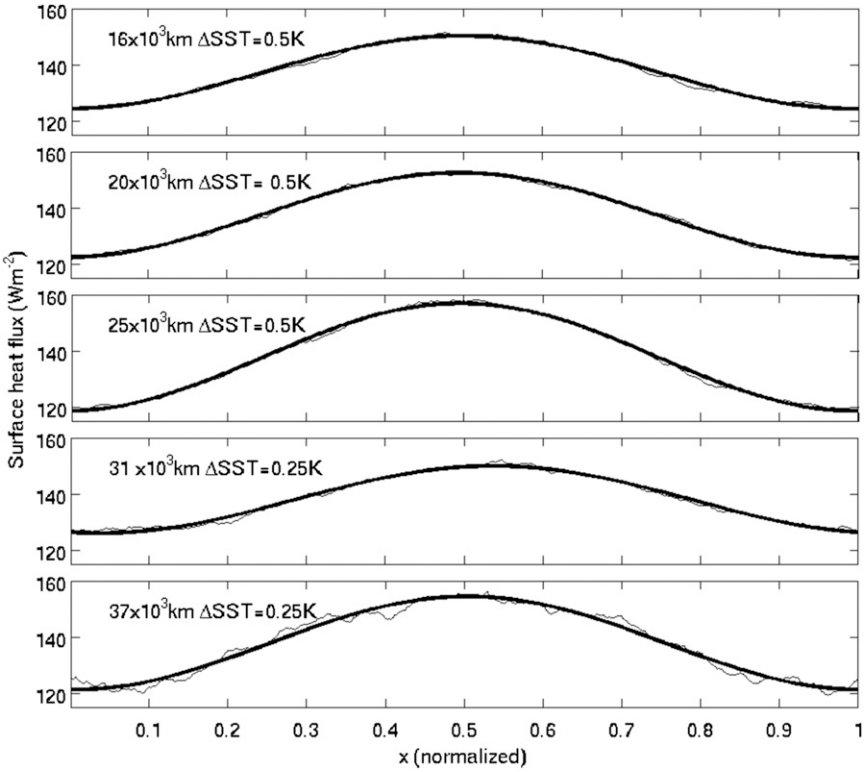

FIG. 5. As in Fig. 4, but for surface heat (latent + sensible) fluxes.

4. Linear response functions of temperature, moisture, and momentum

First, we use the method of Kuang (2010) to construct linear response functions of the cumulus ensemble, which summarize how collective effects of the cumulus ensemble vary around a reference mean state. In our Walker cell, large-scale horizontal winds are limited to the long (x) dimension, so we include only the x-direction winds (or u) and neglect the y-direction winds. Cross shear is thus not considered here. We run the CSRM with the same setup as in the Walker cell experiments with 2-km horizontal resolution, except with a uniform SST of 28°C and smaller domain sizes. We have calculated the linear response functions for two horizontal domain sizes: one is 128 km × 128 km (hereafter the 128-km case) and the other is 2048 km in the x direction and 64 km in y (hereafter the 2048-km case). To reduce the computational burden, we use 28 instead of 64 vertical layers in the 2048-km case, with the vertical resolution varying from 100 m near the surface to 1 km in the middle and upper troposphere. To assess the effect of differing vertical resolutions, we have further constructed the linear response functions for a 28-layer 128 km × 128 km case. The results, shown in Fig. 8, are similar to those with 64 layers. Having both the 128-km and the 2048-km cases allows us to assess the effect of convective organization: inspection of snapshots (not shown) indicates that the 128-km case features mostly unorganized convection while the 2048-km case features organized convection similar to that shown in Fig. 2. Specifics of the linear response function construction are described in appendix A, along with a test that shows their adequacy. For our reference state of zero large-scale horizontal wind, by symmetry, the cross terms between u and the thermodynamic variables should be zero in theory and are indeed small in practice and have little effect on our results. We shall therefore neglect these cross terms, and refer to the thermodynamic portion of matrix $\mathbf{G}$ as $\mathbf{M}$ and the u portion as $\mathbf{L}$.

The three columns of Fig. 8, from left to right, are results from the 64-layer 128-km case, the 28-layer 128-km case, and the 2048-km case, respectively. Figures 8a–d show the quadrants of $[\exp(\mathbf{M}\Delta t) - \mathbf{I}]/\Delta t$, where Δt is 4 h, and $\mathbf{I}$ is the identity matrix, and Fig. 8e shows $[\exp(\mathbf{L}\Delta t) - \mathbf{I}]/\Delta t$. In other words, each column shows the 4-h average tendencies associated with T, q, and u anomalies in an individual layer, the pressure of which is shown on the x axis. We have normalized each column of the matrices by the mass of the perturbed layer. We show 4-h averages instead of instantaneous tendencies because the latter are dominated by the fastest decaying eigenmodes and more prone to error, as described in Kuang (2010). These fast

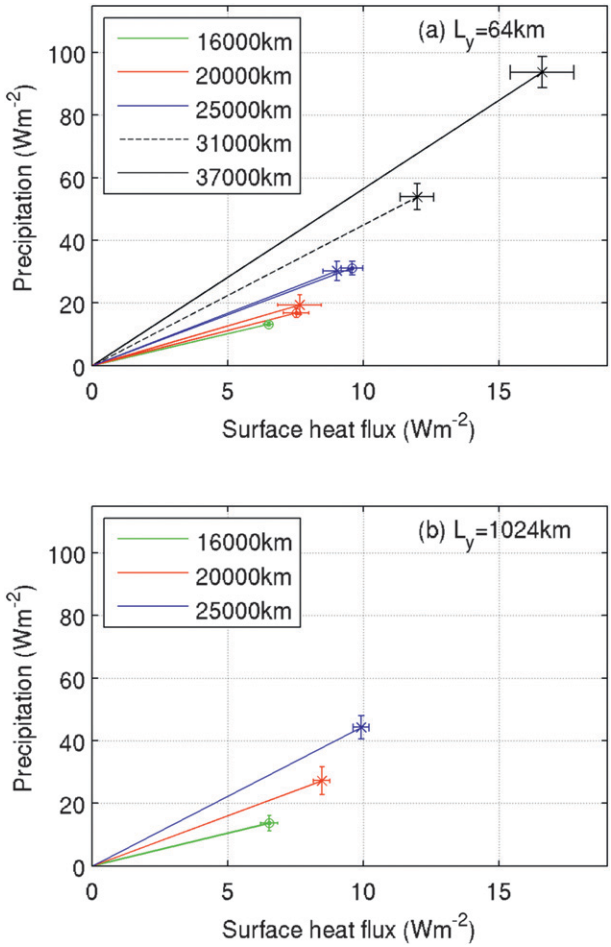

FIG. 6. Coefficients of the first Fourier component of precipitation and surface heat flux for Walker cells of different domain sizes.

decaying eigenmodes, while dominant in the instantaneous tendencies, decay so fast that their precise decay rates do not significantly affect the interaction of convection with the large-scale flow. The 4-h averaging time reduces the dominance of these fast-decaying eigenmodes, yet is short enough that the tendencies can still be ascribed mostly to localized anomalies.

The tendencies for the two 128-km cases show broad similarity. A warm anomaly in the subcloud layer (below about 900 hPa) leads to cooling locally and warming over the rest of the column (Fig. 8a). With a warm anomaly in the lower half of the subcloud layer, there is more overturning in the subcloud layer, which dries its lower half and moistens the upper half (Fig. 8b). A warm anomaly in the upper half of the subcloud layer has the opposite effect. Effects of temperature and moisture anomalies in the free troposphere are broadly consistent with a parcel view of moist convection (Figs. 8a–d): a warm anomaly forms a buoyancy barrier that eliminates some of the convective updraft parcels, leading to cooling at and above the perturbed layer, while a moist anomaly reduces the degree of entrainment drying experienced by the parcels and allow them to reach higher, leading to warming at and above the perturbed layer. Heating response to moisture anomalies in the midtroposphere seems somewhat higher in the 64-layer case, although greater signal-to-noise ratios would be needed to establish this. These responses are broadly consistent with those from previous studies (Kuang 2010; Tulich and Mapes 2010).

Responses to temperature and moisture anomalies in the 2048-km case, where convection is organized, however, have some striking differences. Here, a warm anomaly above about 600 hPa leads to cooling of the entire free troposphere and warming of the subcloud layer, as well as moistening of the free troposphere, particularly the lower troposphere above the subcloud layer (Figs. 8a,b). A warm anomaly between 900 and 600 hPa, on the other hand, has the opposite effect. Temperature anomalies in the subcloud layer appear to produce little heating/cooling anomalies in the free troposphere. A moist anomaly in either the lower or the upper troposphere leads to warming of the entire free troposphere, while warming anomalies associated with moist anomalies in the midtroposphere tend to be smaller (Fig. 8c). The general behavior here is consistent with a layer mode convective overturning, a view advocated in Kingsmill and Houze (1999) and Mechem et al. (2002), as well as in the analytical model of Moncrieff (1992). In the 2048-km case, there is strong convective organization with deep inflows such that air rising to the upper troposphere comes from a much deeper layer than the subcloud layer. With this layer mode convective overturning, convective heating is strengthened when air in the deep inflow is warmer and moister and weakened when the air above 600 hPa is warmer, indicating stronger stability. The manifestation of the parcel versus layer mode of convective overturning in the linear response functions is very interesting and will be studied in more detail in the future.

The linear response functions for u momentum shown in Fig. 8 are more similar among the different cases. They are for the most part dominated by near diagonal terms. The main difference is that subcloud-layer u anomalies give rise to tendencies in the whole column in the 64-layer case but not in the 28-layer cases, indicating a dependence on vertical resolution. We do not pursue this difference in this paper because it has little effect on the behavior of the weakly forced Walker cells. In the free troposphere, there is clear downward advection of the u anomalies. Such a tendency is well known and has been associated with the compensating subsidence induced by convective updrafts and has been represented in cumulus parameterization schemes as such (e.g.,

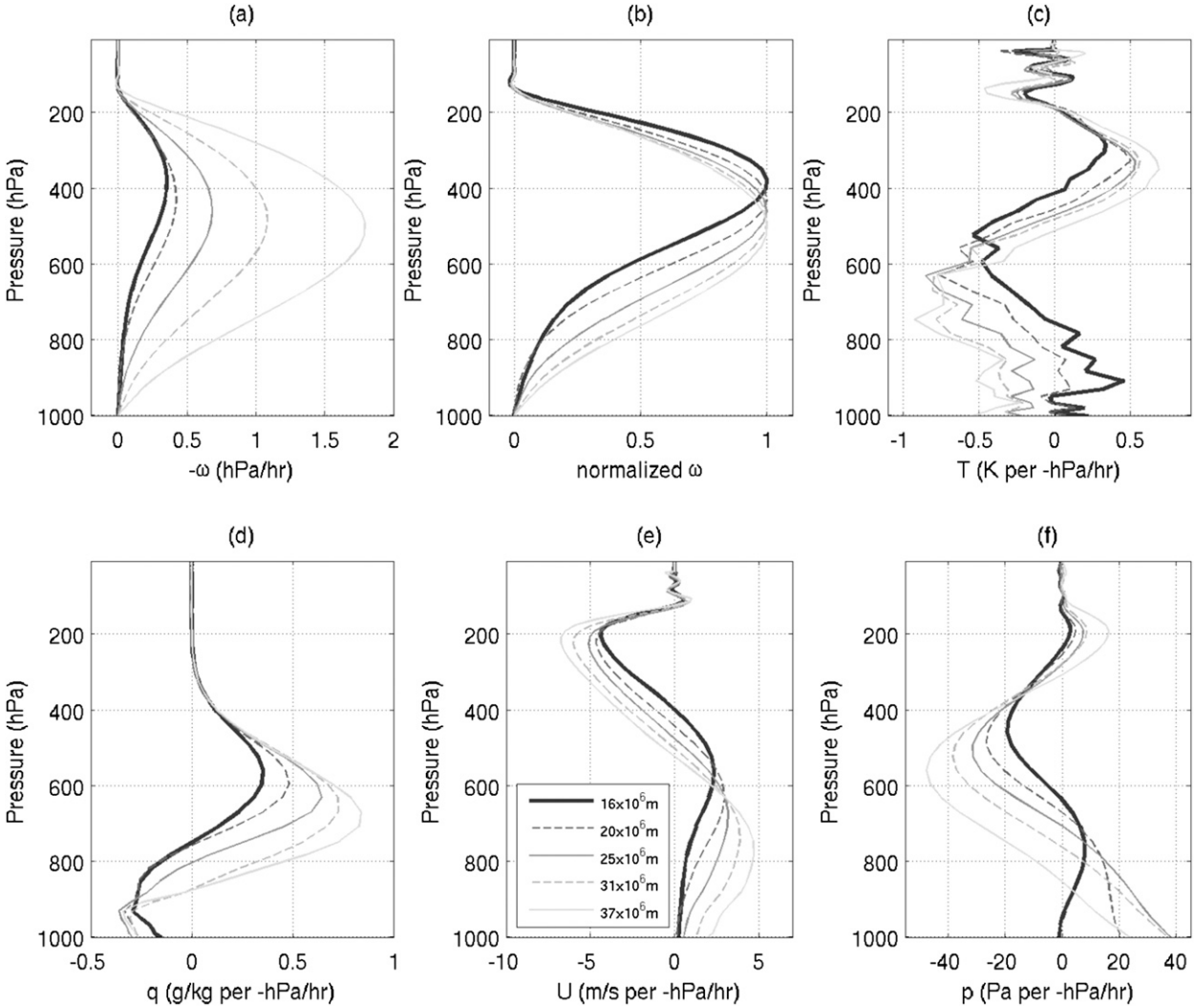

FIG. 7. Vertical profiles of (a) pressure velocity, and normalized (b) pressure velocity, (c) temperature, (d) specific humidity, (e) u velocity, and (f) perturbation pressure from the Walker runs with a y dimension of 64 km. Profiles in (b)–(f) are normalized by the maximum pressure velocity of each case. Profiles for u are at a quarter length of the domain ($x = A/4$), and profiles of all other variables are at the center of the domain ($x = A/2$). Sizes of the x dimension are given in (e). For the 16 000-, 20 000-, and 25 000-km cases, a ΔSST of 0.5°C was used and results were divided by 2 for comparison with the other two cases, which used a ΔSST of 0.25°C.

Schneider and Lindzen 1976; Zhang and Cho 1991; Wu and Yanai 1994; Gregory et al. 1997; Mapes and Wu 2001).

To quantify the convective momentum tendencies seen in Fig. 8, we use a localized representation that includes Rayleigh damping, vertical advection, and diffusion:

$$-\varepsilon u' + \eta u'_z + (\kappa u'_z)_z, \tag{4}$$

where ε, η, and κ represent the strength of these three components, respectively, and the primes indicate an anomaly. A positive η here indicates downward advection. We have estimated ε, η, and κ as a function of height by approximating the advection and diffusion operators using a three-point stencil and matching the three values centered on the main diagonal of matrix **L**.

The estimated parameters are shown in Fig. 9. The Rayleigh damping coefficient ε is large in the subcloud layer, with a damping time scale of 2 h (Fig. 9a). This is associated with surface friction and rapid momentum exchange in the subcloud layer. The shape of η (Fig. 9b) resembles that of the compensating subsidence in the bulk of the troposphere, which is computed by dividing the cloud updraft[2] mass flux by density (Fig. 9d), consistent

[2] Defined as grid points with cloud condensates greater than 0.01 g kg^{-1} and vertical velocity greater than 0.

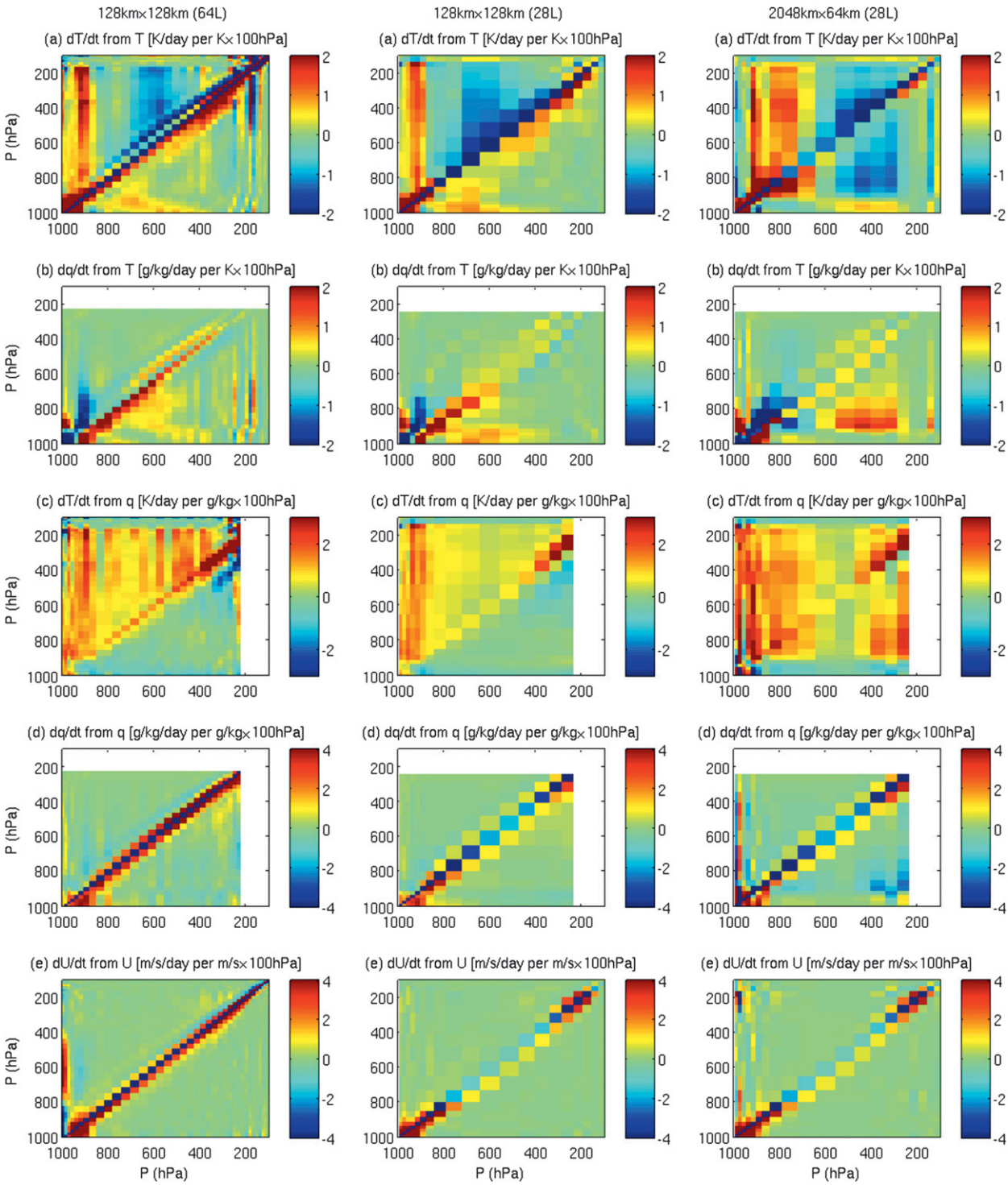

FIG. 8. The 4-h average linear response functions for the (left) 64-layer 128-km, (middle) 28-layer 128-km, and (right) 2048-km cases. (a)–(d) The quadrants of the linear response functions for temperature and moisture and (e) the linear response function matrix for u velocity (see text for more explanations). The horizontal axis is the pressure of the perturbed layer, and the vertical axis is the pressure of the responding layer. Each column of the matrices is normalized by the mass of the perturbed layer.

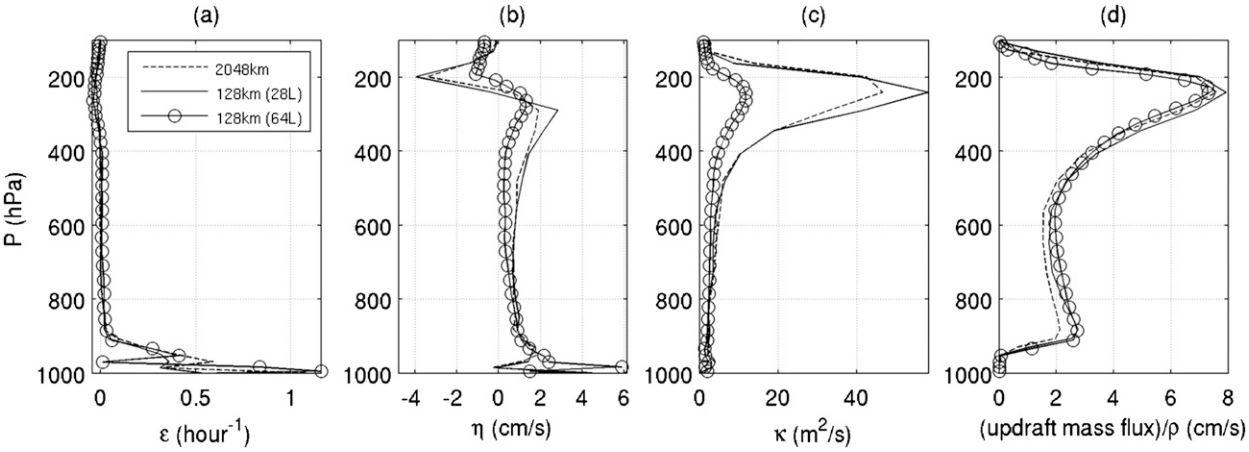

FIG. 9. Vertical profiles of the estimated parameters (a) ε, (b) η, and (c) κ, as well as (d) the cloud updraft mass flux divided by density for the three limited domain cases: the 64-layer 128-km case (circles), the 28-layer 128-km case (solid), and the 2048-km case (dashed).

with the view that compensating subsidence is responsible for the downward advection of momentum. The η values are smaller than those of the compensating subsidence. This, at face value, is consistent with the treatment of reducing the u velocity tendency associated with compensating subsidence to account for the effect of pressure gradient terms (e.g., Gregory et al. 1997). We caution that such inferences from Fig. 9 or alike are subject to ambiguities in the definition of updraft mass flux; a more (or less) restrictive definition of cloud updrafts would have given a smaller (or greater) compensating subsidence. Such ambiguities stem from the approximation implicit in separating the convective circulation into a cloud updraft mass flux and compensating subsidence and assuming that properties are homogeneous within each category. The rapid variations in ε and η in the subcloud layer in the 64-layer case are sensitive to uncertainties in the constructed $\mathbf{L}$. The diffusivity κ is large in the upper troposphere, although its values become smaller with the higher vertical resolution, suggesting the influence of numerical diffusion. There are some unphysical values such as positive Rayleigh damping in the upper troposphere, indicating that a local operator may not always be suitable for CMT.

We shall further note that the localized approximations are not quantitatively accurate despite the dominance of near-diagonal terms in $\mathbf{L}$. This is because that $\mathbf{L}$ emphasizes the fastest-decaying eigenmodes, which tend to have strong local components. However, for coupling with large-scale circulations, the more slowly decaying eigenmodes masked in $\mathbf{L}$ are important. Additional discussions and illustrations of this point are presented in appendix B.

5. Parameterizing large-scale dynamics

As the second simplification of the system, we parameterize the large-scale dynamics based on linearized large-scale equations. This is well justified for the present weakly forced Walker cell problem. In pressure coordinate, linearized perturbation equations of momentum, continuity, and hydrostatic balance can be written as

$$u'_t = -\varphi'_x + Lu', \tag{5}$$

$$u'_x + \omega'_p = 0, \tag{6}$$

$$\varphi'_p = -\frac{\theta'}{\bar{\rho}\bar{\theta}}, \tag{7}$$

where φ is the geopotential, L is a linear operator acting on u' so that Lu' gives the perturbation convective tendency for u velocity, and all other symbols assume their usual meteorological meaning with the background variables denoted with an overbar and the perturbation variables denoted with a prime.

Treating a single horizontal wavenumber k at a time, eliminating $\varphi'$and u' from Eqs. (5)–(7) [see Kuang (2008) for details], and taking the steady state, we have

$$[L(\omega')_p]_p = -k^2\frac{\theta'}{\bar{\rho}\bar{\theta}}, \tag{8}$$

where ω' is the large-scale pressure velocity and θ' is the departure of the horizontally averaged potential temperature over the limited domain model from the reference profile (virtual effect is accounted for in the actual calculation). While Rayleigh damping (i.e.,

$L = -\varepsilon$) was used previously (Kuang 2008; Blossey et al. 2009; Kuang 2011), CMT is known to be more complicated (e.g., Schneider and Lindzen 1976; LeMone 1983; Soong and Tao 1984; Zhang and Cho 1991; Moncrieff 1992; Wu and Yanai 1994; Gregory et al. 1997; Robe and Emanuel 2001; Mapes and Wu 2001; Tung and Yanai 2002a,b, among many others), as also shown in section 4. We will use the CSRM-derived linear response matrix to represent CMT. To gain insights into how CMT affects the large-scale flow, we will also use three idealized forms of CMT and $L = \kappa\partial^2/\partial z^2$, with ε, η, and κ values that are constant in height. As is clear from Eq. (8), the solution only depends on the ratios of these values to k^2. For $L = -\varepsilon$, rigid lid boundary conditions are used at the surface and at the model top. With $L = \eta\partial/\partial z$, an additional no-slip boundary condition is imposed at the upper boundary, while with $L = \kappa\partial^2/\partial z^2$, a no-slip lower boundary condition is further enforced.

We will also examine the relaxation or WTG approach, which computes the large-scale vertical velocity as follows:

$$\omega' = \frac{\theta'}{\tau(d\overline{\theta}/dp)}, \tag{9}$$

where τ is the relaxation time scale. In this way, adiabatic cooling associated with the large-scale vertical motion relaxes the horizontally averaged potential temperature in the limited domain model toward the reference profile with a time scale of τ. We will set $1/\tau$ constant with height in the free troposphere and decrease it linearly to zero from the top of the boundary layer (set to 1 km) to the surface, similar to Wang and Sobel (2011).

6. Response of the coupled system to SST forcing

We now examine how the coupled system of the large-scale flow interacting with cumulus convection responds to SST forcing. Representing convective heating and moistening using the linear response function matrix **M**, we can write the steady-state temperature and moisture equations as

$$0 = \mathbf{M}\begin{pmatrix}\theta' \\ q'\end{pmatrix} - \begin{pmatrix}\omega'\dfrac{d\overline{\theta}}{dp} \\ \omega'\dfrac{d\overline{q}}{dp}\end{pmatrix} + \begin{pmatrix}F_\theta \\ F_q\end{pmatrix}, \tag{10}$$

where F_θ and F_q are the imposed forcings in θ and q, respectively. Together with the parameterized large-scale dynamics [Eq. (8)] and representing operator L with the linear response function matrix **L**, we can solve for responses of θ', q', and w' to forcing as a matrix problem. Note that Neelin and Yu (1994) and Yu and Neelin (1994) examined an unforced version of this problem, using the Betts–Miller scheme instead of the CSRM-derived matrices used here.

To compute F_θ and F_q, we first use the bulk formula to compute the anomalous surface sensible and latent heat fluxes due to a ΔSST of 0.25 K and a corresponding 0.37 g kg^{-1} increase in surface saturation specific humidity. These are surface heat flux anomalies due solely to changes of the ocean surface and do not include those due to surface air temperature and moisture anomalies, effects of which are included in the matrix **M**. The anomalous surface fluxes are then uniformly deposited in the lowest three model layers to give F_θ and F_q. Changing the number of layers over which the anomalous fluxes are deposited has little effect on the solution in the 128-km cases, but it does cause minor changes in the 2048-km case because of greater uncertainties in the **M** derived for that case.

The results for the 64-layer 128-km case are shown in the leftmost column of Fig. 10. Results for the 28-layer 128-km case are similar and omitted. The pressure velocity field (Fig. 10a) shows significant variations with horizontal wavelength. These variations are partly due to changes in the shape of the vertical velocity (Fig. 10b) and partly due to changes in the surface heat fluxes (Fig. 10c).

The shape of the vertical velocity profiles, shown as the normalized pressure velocity profiles (with a maximum absolute value of one) in Fig. 10b, undergoes systematic changes with horizontal wavelength. At wavelengths shorter than 1000 km, there is a strong positive peak around 250 hPa and a weak positive peak near 900 hPa. As horizontal wavelength increases, the upper peak descends and the lower peak diminishes. For horizontal wavelengths between 4000 and 12 000 km, the profile takes a second baroclinic structure, with a positive peak near 350 hPa and a negative peak near 700 hPa. Such a profile allows for efficient export of column moist static energy, leading to a large increase in GMS [defined in Eq. (3)], with a peak value of 3, which exceeds our plotting range. As the horizontal wavelength increases further, the vertical velocity profile changes into a first baroclinic structure peaking near 500 hPa, and the GMS decreases toward zero. Surface fluxes also increase rapidly as the wavelength approaches 22 000 km. This, combined with the decrease in GMS, leads to a rapid strengthening of the resulting Walker circulation. For wavelengths longer than 22 000 km, the unforced system (with F_θ and F_q equal to 0) becomes unstable and the response switches sign, which implies that the steady-state solution sought in Eq. (10) is no longer realizable.

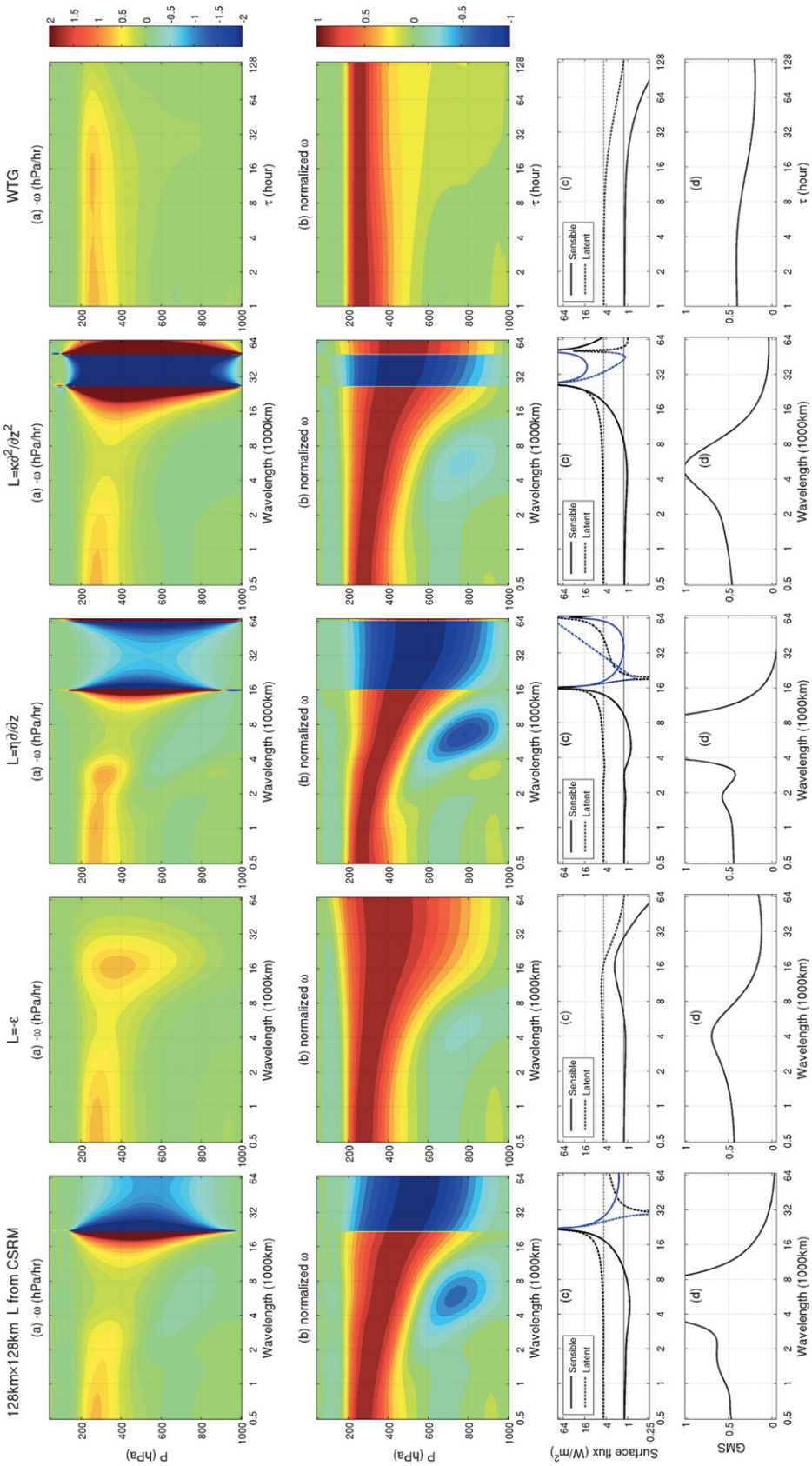
128km×128km L from CSRM
L=-ε
L=η∂/∂z
L=κ∂²/∂z²
WTG
(a) -ω (hPa/hr)
(b) normalized ω
(c)
(d)
Sensible
Latent
P (hPa)
Surface flux (W/m²)
GMS
Wavelength (1000km)
τ (hour)

Results for the 2048-km case (Fig. 11, left column) also show significant variations with horizontal wavelength (note that the scale in Fig. 11a is different from that of Fig. 10). At the shortest horizontal wavelengths shown, the shape of the vertical velocity profiles also has two peaks, one around 300 hPa and another near 800 hPa. Compared to the 128-km case, the peak in the lower troposphere is more pronounced. As the horizontal wavelength increases, the upper peak descends and the lower peak diminishes, as in the 128-km case. For horizontal wavelengths between 8000 and 16 000 km, there is a sizable second baroclinic component on top of a first baroclinic structure so that vertical velocity peaks around 400 hPa and is slightly negative in the lower troposphere. The second baroclinic structure, however, is not nearly as pronounced as that seen in the 128-km case at horizontal wavelengths between 4000 and 12 000 km. As the horizontal wavelength further increases, the vertical velocity becomes dominated by a first baroclinic structure peaking at 550 hPa. There are also significant variations in surface heat fluxes.

To compare with the explicit Walker experiments (Fig. 7), we show similar plots for the 128-km case (Fig. 12) and the 2048-km case (Fig. 13). The increase in circulation strength with horizontal wavelength is clearly too strong in the 128-km case, as can already be seen in Fig. 10. The 2048-km case is in closer agreement but the increase in circulation strength with horizontal wavelength is still slightly too strong. The temperature and moisture anomalies in the 2048-km case are in good agreement with results from the explicit Walker simulations, capturing both the overall structures and their variations with horizontal wavelength that were described in section 3. On the other hand, while the 128-km case captures some of the features such as the warm anomaly in the upper troposphere and the cold anomaly in the lower troposphere, moister free troposphere but drier boundary layer, and the higher surface pressure (note that all of these are over the warmer SSTs), it has little moistening of the free troposphere as horizontal wavelength increases. These results indicate that our simplified system can reproduce the behavior of the Walker circulation, provided that the constructed linear response functions account for the convective organization seen in the Walker cells. The dependence of the Walker cell on the degree of convective organization will be explored in the next section.

7. Dependence on convective organization

The most prominent difference between the 2048- and the 128-km cases is that the second baroclinic mode structure is weak in the 2048-km case. This is true at short horizontal wavelengths (shorter than 4000 km), where the lower troposphere peak is more comparable with the upper troposphere peak in the 2048-km case. It is also true at intermediate wavelength ranges (4000–12 000 km), where the 128-km case has a much more pronounced second mode structure. This leads to the generally lower GMS in the 2048-km case.

The differing behaviors between the 128-km and the 2048-km cases are mainly caused by differing sensitivities of convective heating/moistening to temperature and moisture anomalies, described by the **M** matrix. We have made experiments using the **M** matrix, from the 28-layer 128-km case and the **L** matrix, which describes CMT, from the 2048-km case, and found that the results (not shown) are similar to those in Fig. 10. On the other hand, using the **M** matrix from the 2048-km case and the **L** matrix from the 28-layer 128-km case gives results similar to those shown in Fig. 11.

The reason for the weaker second baroclinic mode structure in the 2048-km case is the following. Because of layer mode convective overturning, convective heating in response to temperature and moisture anomalies is predominantly of the same sign throughout the free troposphere (section 4). Therefore, there is little second baroclinic mode convective heating that can balance the adiabatic cooling/warming associated with a second baroclinic structure in vertical velocity, limiting the amplitude of the latter.

The difference in the thermodynamic structure can be explained similarly. In Figs. 12 and 13, it was seen that as horizontal wavelength increases, the free-tropospheric moistening is much more pronounced in the 2048-km case than in the 128-km case. In the 128-km case, as

←

FIG. 10. The response of Walker cells to a $\Delta SST = 0.25°C$ forcing for a range of horizontal wavelengths computed using the simplified system with the linear response functions from the 64-layer 128-km case. The columns are (from left to right) results with **L**, the linear response functions for momentum derived from the CSRM, $L = -\varepsilon$, $L = \eta\partial/\partial z$, $L = \kappa\partial^2/\partial z^2$, and with the relaxation/WTG approach. The different rows are (a) pressure velocity, (b) normalized pressure velocity, (c) absolute values of surface heat fluxes, and (d) the gross moist stability. The horizontal wavelength and the surface heat fluxes are shown in logarithmic scale. The blue curves in (c) indicate negative values of surface heat fluxes.

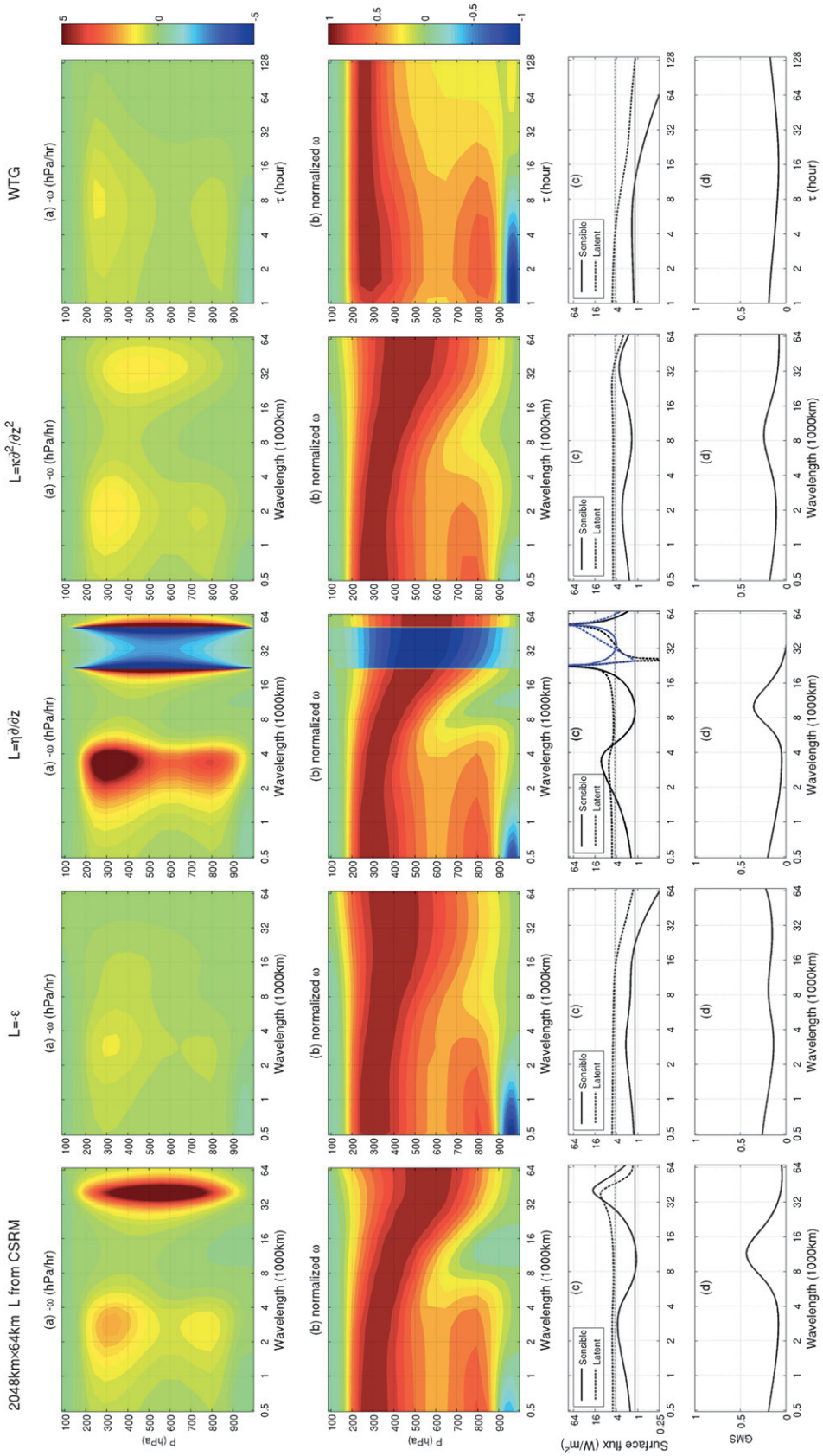

FIG. 11. As in Fig. 10, but for the 2048-km case and a different color scale in (a).

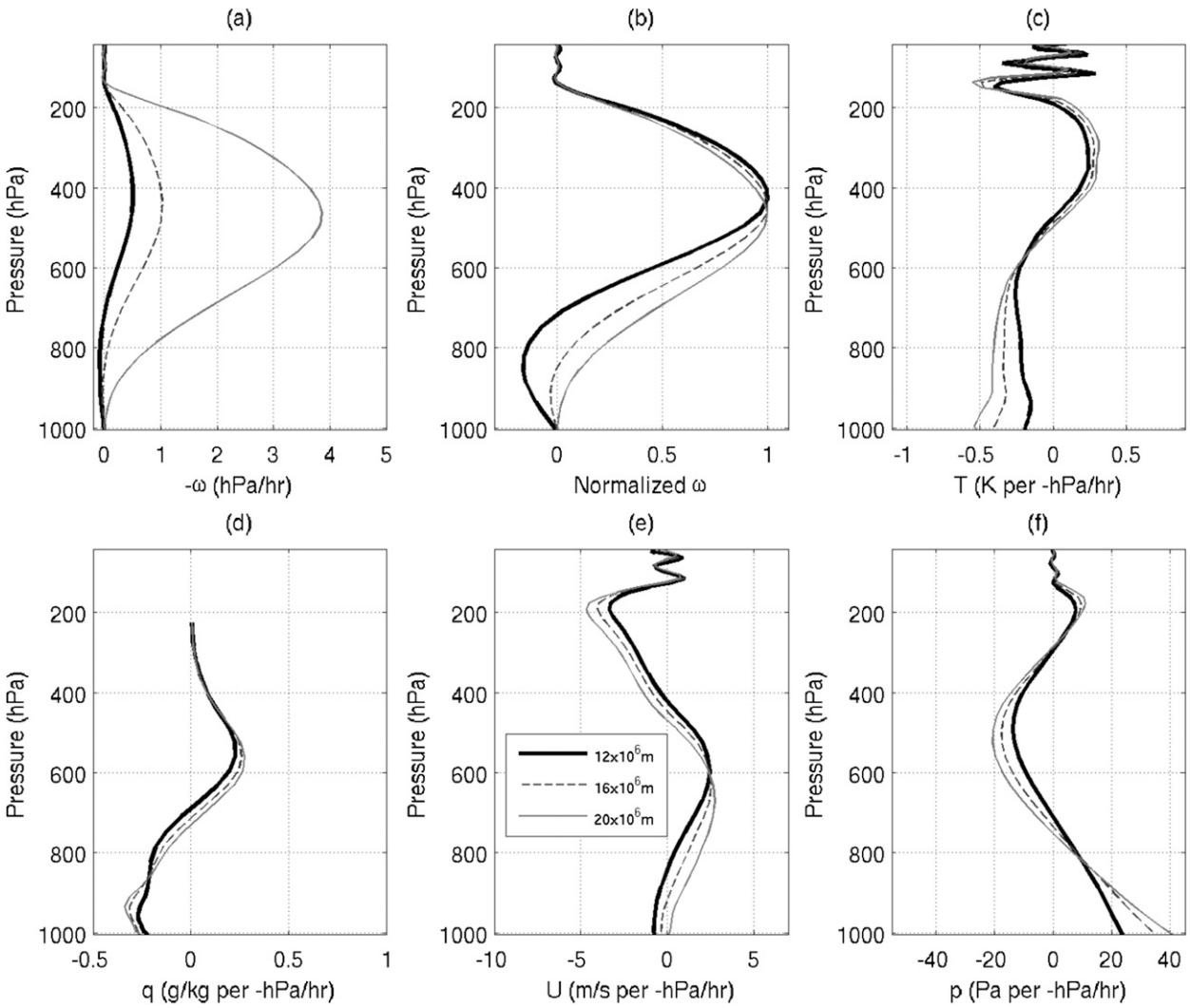

FIG. 12. As in Fig. 7, but for the simplified system with the linear response functions from the 64-layer 128-km case.

horizontal wavelength increases, the lower troposphere develops a stronger cold anomaly, which appears sufficient to shift convective heating toward a less-top-heavy profile, balancing the less-top-heavy vertical velocity profiles. In the 2048-km case, as horizontal wavelength increases, the lower troposphere also develops a stronger cold anomaly. However, in addition to local convective heating, this cold anomaly also leads to anomalous cooling over the rest of the free troposphere because of the layer mode convective overturning. A moister free troposphere is thus needed to maintain sufficient convective heating in order to balance adiabatic cooling over the free troposphere associated with the vertical motion.

Notwithstanding the difference between the 128- and 2048-km cases, there is a tendency in both cases for structures with shorter vertical scales to diminish as the horizontal wavelength increases. While a third baroclinic mode is evident at our shortest horizontal wavelengths, it vanishes at intermediate horizontal wavelengths leaving only the second and first baroclinic modes. At our longest wavelengths, the second baroclinic mode also vanishes, and the vertical velocity profile is dominated by a first baroclinic mode structure.

8. The role of convective momentum transport

In Figs. 10 and 11, we show behaviors of the coupled system with four idealized treatments of the momentum equation. The first three are based on the gravity wave approach [Eq. (8)] with $L = -\varepsilon$ with $\varepsilon = 1$ day^{-1} (second columns), $L = \eta\partial/\partial z$ with $\eta = 0.01$ m s^{-1} (third columns), $L = \kappa\partial^2/\partial z^2$ with $\kappa = 20$ m^2 s^{-1} (fourth columns), and

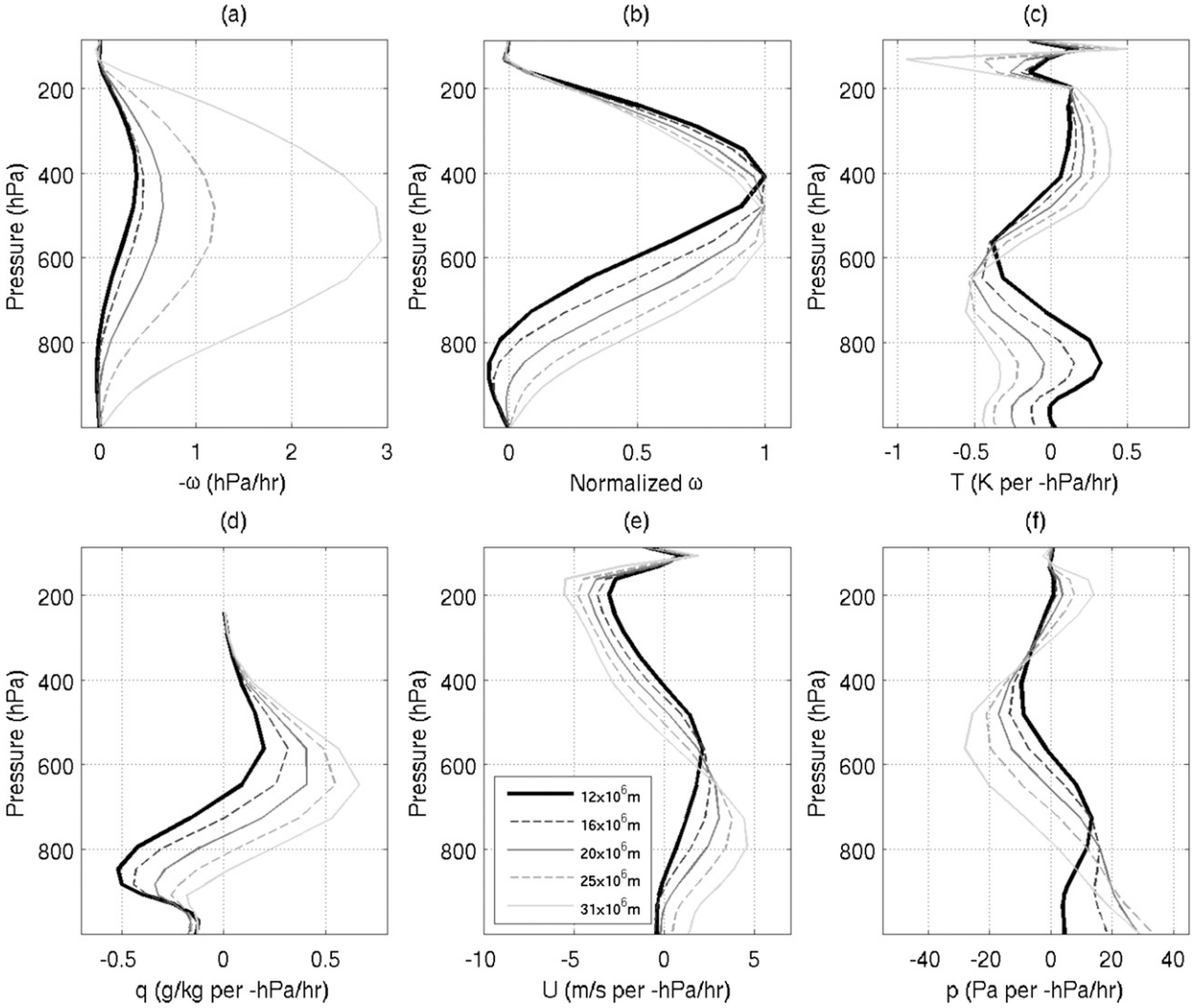

FIG. 13. As in Fig. 7, but for the simplified system with the linear response functions from the 2048-km case.

the fourth is the relaxation or WTG approach (fifth columns). The boundary conditions are those described in section 5.

Figures 14 and 15 illustrate the differences in the thermodynamic structures with the four idealized treatments of the momentum equation by showing normalized pressure velocity, temperature, and specific humidity profiles for a few selected horizontal wavelengths and relaxation time scales for the 2048-km case. The 25 000-km case is not shown for the downward momentum advection case because the unforced problem is unstable so that there is no steady-state solution. Results from the 128-km case show similar dependences on CMT even though individual profiles are different and are omitted here.

We shall now interpret variations of the weakly forced Walker cells with horizontal domain size and examine the role of CMT. Let us write the solution to Eq. (8) as the sum of individual eigenmodes of the operator $[L(\cdots)_p]_p$ on its left-hand side (lhs) so that

$$\omega' = \sum_m \omega_m \psi_m(p), \tag{11}$$

with the right-hand side (rhs) expressed as

$$\frac{\theta'}{\overline{\rho}\overline{\theta}} = \sum_m \theta_m \psi_m(p), \tag{12}$$

where $m = 1, 2, \ldots$ are the mode number and $\psi_m(p)$ is the mth eigenmode. Equation (8) therefore becomes

$$\nu_m \omega_m = -k^2 \theta_m, \tag{13}$$

where ν_m is the mth eigenvalue.

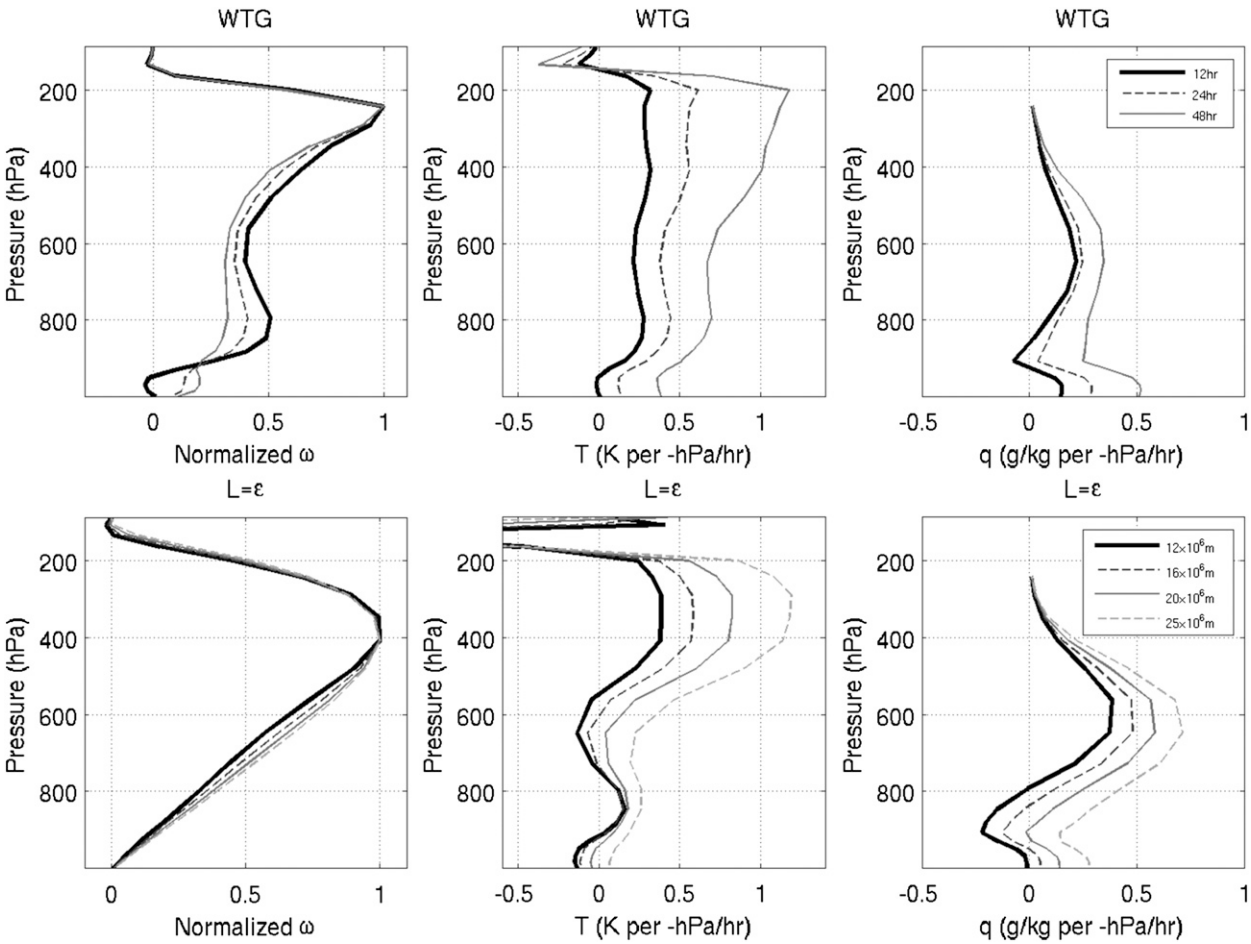

FIG. 14. Profiles of (left) normalized pressure velocity, (middle) temperature, and (right) specific humidity, using linear response functions for temperature and humidity from the 2048-km case, together with (top) the relaxation/WTG approach and (bottom) Rayleigh momentum damping. The legend of each row is given in the right column.

Figures 16a–c show the eigenmodes of $[L(\cdots)_p]_p$ with $L = -\varepsilon$, $L = \eta\partial/\partial z$, and $L = \kappa\partial^2/\partial z^2$, with constant values of ε, η, and κ (and boundary conditions described in section 5). In Figs. 16d and 16e, we also show the real component of the eigenmodes with the CSRM-derived L from the 28-layer 2048-km and 128-km cases (the eigenmodes from these cases can appear as complex conjugate pairs). Using absolute values gives very similar results. The general features in Fig. 16e are unchanged when the 64-layer 128-km case is used, but the high amplitudes near 100 hPa for mode 6 disappear, indicating that this particular feature is not robust. The normalized eigenvalues are shown in Fig. 16f. Since the eigenvalues with the CSRM-derived L can be complex, values shown are again the real component. While the finite model top artificially produces discrete vertical modes, the model top is high enough that the modes are sufficiently continuous. Two features are germane to the present discussion. First, modes with shorter vertical scales have larger eigenvalues. Among the three idealized cases, as the vertical scale decreases, the eigenvalue increases at a rate that is fastest with $L = \kappa\partial^2/\partial z^2$ and slowest with $L = -\varepsilon$, a result directly associated with the order of the derivative. The rate of increase is more variable with the two CSRM-derived L but is broadly similar to that with $L = \kappa\partial^2/\partial z^2$. Second, the eigenmodes with$L = \eta\partial/\partial z$ have greater amplitudes in the lower troposphere, so do eigenmodes with the CSRM-derived L.

All gravity-wave-equation-based treatments of the momentum equation (first through fourth columns of Figs. 10 and 11) show the general tendency for the vertical velocity profiles of the Walker circulation to move toward broader vertical scales at large horizontal scales: as horizontal wavelength increases, we see the general trend of diminishing third and then second baroclinic structures, leaving a mostly first baroclinic structure at very long wavelengths. The basic reason for this general tendency was given in Kuang (2011), where a simple

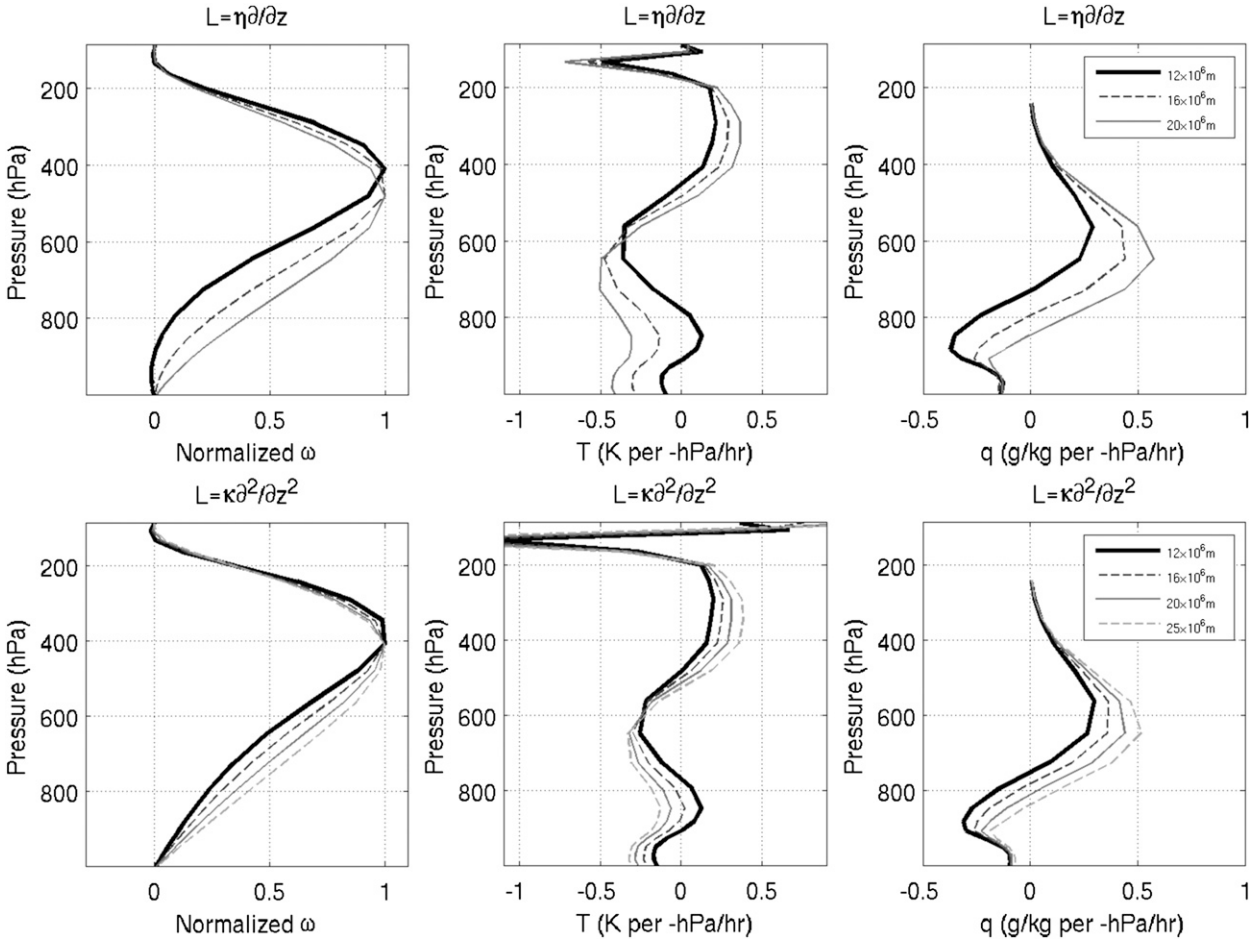

FIG. 15. As in Fig. 14, but for (top) downward momentum advection and (bottom) diffusive momentum damping.

model was constructed to illustrate the behavior, along with a schematic (Fig. 7 in that paper). Below, we extend the arguments to the full matrix problem of Eq. (10).

In the limit of short horizontal wavelengths, the temperature anomalies required to maintain the large-scale circulation against momentum dissipation are sufficiently small that they have negligible effect on convection. Therefore, θ' can be set to zero in Eq. (10) so that Eq. (10) can be solved without reference to Eq. (8), and Eq. (8) will only be used to compute θ' after ω' has been computed. This is the basic premise of the WTG thinking (Sobel and Bretherton 2000). Indeed, results at the shortest wavelengths shown in Figs. 10 and 11 are similar across the disparate treatments of the momentum equation. We should note, however, that this short wavelength limit may not be realizable as a linear Walker cell problem because of the nonlinear effect noted at the end of section 3.

As the horizontal wavelength increases, the ratio of θ' to $-\omega'$ increases [Eq. (8)]. When the required temperature anomalies become large, so will the convective tendencies [the first term on the rhs of Eq. (10)]. Since the sum of the first and the second rhs terms in Eq. (10) must balance the imposed forcing, the amplitude of ω' will be limited when the ratio of θ' to ω' becomes sufficiently large. Because the eigenvalues ν_m increase with the mode number, the temperature anomalies required to maintain a vertical velocity anomaly of given amplitude are greater for the higher vertical modes (i.e., those with smaller vertical scales) [Eq. (13)]. Therefore, these shorter vertical modes are limited more strongly so that modes with broader vertical scales will become more dominant as the horizontal wavelength increases. Temperature structures that invoke large convective tendencies (i.e., those project onto the fast decaying eigenmodes of $\mathbf{M}$) are also limited more strongly, again because the sum of the first and the second rhs terms in Eq. (10) must balance the imposed forcing. Therefore, as the horizontal scale increases, temperature structures that project onto the slowest decaying eigenmodes become more dominant. These two arguments work in concert,

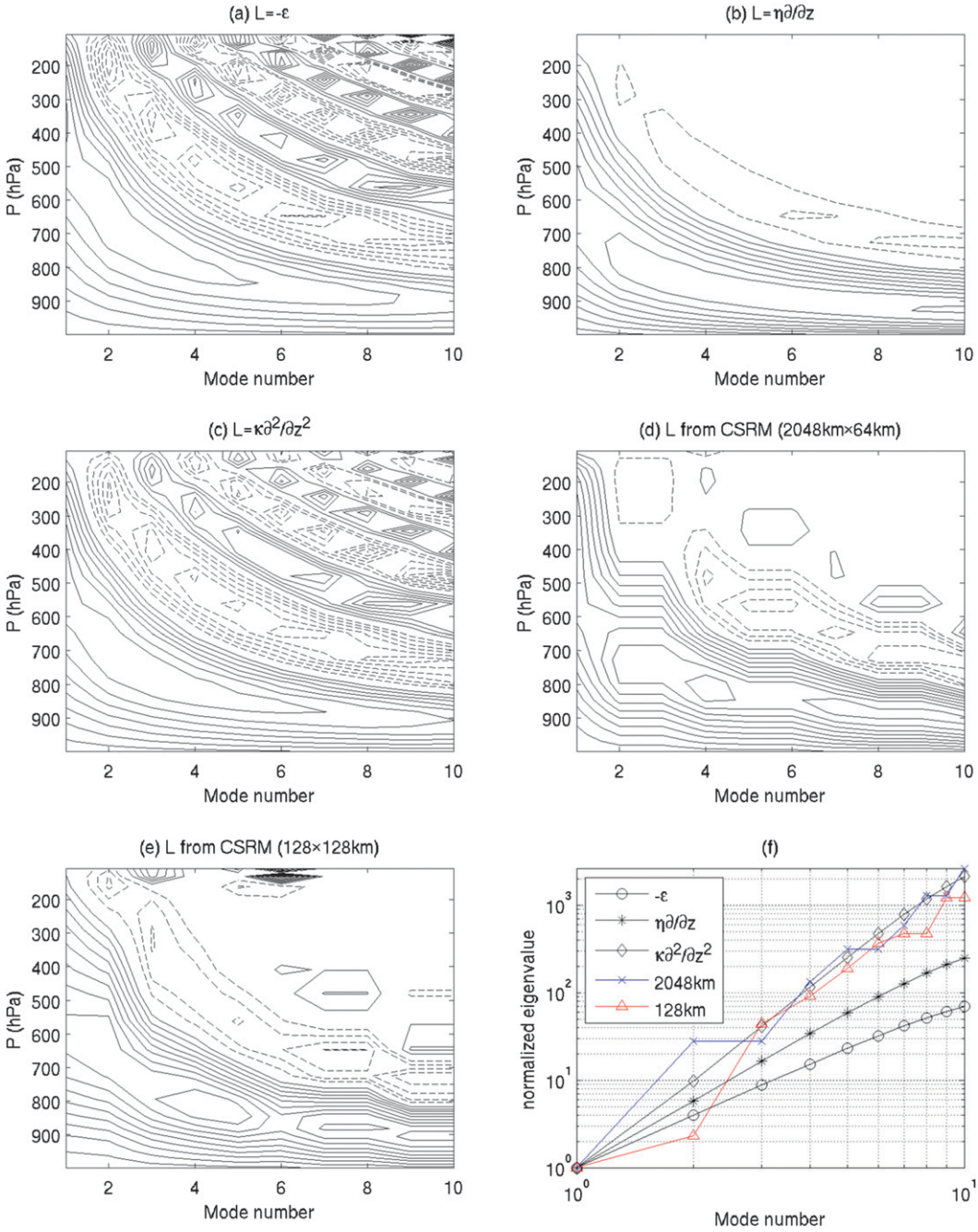

FIG. 16. Eigenmode structures for the operator $[L(\cdots)_p]_p$ with (a) $L = -\varepsilon$, (b) $L = \eta\partial/\partial z$, (c) $L = \kappa\partial^2/\partial z^2$, (d) L from the 2048 km × 64 km CSRM simulations, and (e) L from the 128 km × 128 km CSRM simulations (28 layers). Solid contours indicate positive values, dashed contours indicate negative values, and the zero contour is omitted. The contour interval is 0.05. (f) The eigenvalues, normalized to 1 for mode 1, for the five cases.

as temperature anomalies with shorter vertical scales tend to have higher decay rates and larger convective tendencies.

The WTG or relaxation approach that relaxes all vertical wavenumbers with the same time scale (Wang and Sobel 2011; Sobel and Bretherton 2000; Sobel et al. 2007) is equivalent to neglecting variations in ν_m shown in Fig. 16d, thus treating the horizontal propagation speeds as the same for gravity waves of different vertical scales. Such a treatment is consistent with the spirit of the WTG approximation, which assumes that gravity wave adjustment is fast enough to be approximated as

infinitely fast but underestimates the temperature anomalies required to sustain divergent flows with shorter vertical scales relative to those with broader vertical scales. For planetary-scale phenomena of tens of thousands of kilometers, temperature anomalies required to sustain a given divergent flow are sufficiently large to significantly impact convection, and errors in temperature that result from neglecting variations in ν_m start to impact the solution. In particular, the relaxation approach lacks the mechanism to move toward broader vertical scales at long horizontal wavelengths. As seen in Figs. 10 and 11, while the results are similar to the other cases at short horizontal wavelengths, with the WTG approach the upper-troposphere peak in the vertical velocity profile narrows and shifts upward slightly as the horizontal wavelength increases. We note that the vertical velocity profiles from the 128-km WTG case (not shown here) are similar to those reported in Wang and Sobel (2011).

With Rayleigh damping, ν_m increases with decreasing vertical scale but the rate of increase is relatively small compared to those with downward momentum advection and diffusive momentum damping (Fig. 16f). Therefore, the tendency toward broader vertical scales is not as strong. Compared to results with the CSRM-derived **L** and with downward momentum advection and diffusive momentum damping, the second baroclinic component with Rayleigh damping is considerably weaker at intermediate horizontal wavelengths and the vertical velocity profile at the longest horizontal wavelengths peaks higher in altitude at 400 hPa, instead of about 450–500 hPa. We interpret this as resulting from the weaker eigenvalue variations with vertical scale and hence weaker elimination of the higher vertical modes.

The different temperature structures seen in Figs. 14 and 15 can also be explained by how fast the eigenvalues ν_m change with the vertical scales. The constant ν_m in the WTG approach implies that the temperature anomalies follow the vertical velocity structure and have a strong first baroclinic component with the entire troposphere warming more or less uniformly as the relaxation time scale increases (Fig. 14). With Rayleigh damping, the modest ν_m increase with decreasing vertical scale allows for a second baroclinic component that is considerably stronger than that with the WTG approach, with the upper troposphere warming significantly more than the lower troposphere. But there is still a significant first baroclinic component in the temperature anomaly, especially when the vertical velocity profiles become more and more dominated by a first baroclinic structure (Fig. 14). In both the WTG and the Rayleigh damping cases, the surface air also becomes significantly moister with increasing relaxation time scale and horizontal wavelength (or decreasing coupling strength). Such changes are responsible for the decrease in surface heat fluxes at very long wavelengths/relaxation time scales (see row c in the third and fifth columns of Figs. 10 and 11).

With downward momentum advection and diffusive momentum damping, ν_m is so much smaller for a first baroclinic structure than for the higher baroclinic structures that the temperature anomalies have little first baroclinic component (Fig. 15). As horizontal wavelength increases, the upper troposphere warms and the lower troposphere becomes colder over warmer SST.

The differing eigenmode structures for the different choices of CMT (Fig. 16) also have strong imprints in the resulting Walker circulation. Compared to the eigenmodes of $[L(\cdots)_p]_p$ with $L = -\varepsilon$ and $L = \kappa\partial^2/\partial z^2$, the eigenmodes with $L = \eta\partial/\partial z$ are more bottom-heavy, corresponding to stronger anomalies in the lower troposphere. This gives a cold anomaly in the lower troposphere that is stronger than the warm anomaly in the upper troposphere, similar to what is seen in the explicit Walker simulations (Fig. 7) and with the CSRM-derived **L** (Fig. 13). The stronger cold anomalies in the lower troposphere, through hydrostatic balance, give the high surface pressure over the warmer SST seen in Figs. 7 and 13. With $L = \kappa\partial^2/\partial z^2$, the cold anomaly in the lower troposphere and the warm anomaly in the upper troposphere are of similar magnitude and surface pressure anomalies are small. Therefore, the downward advection aspect of the CMT is responsible for the lower-tropospheric cold anomalies being stronger than the upper-tropospheric warm anomaly and the higher surface pressure over the warmer SSTs that were seen in the Walker cells. Physically, downward momentum advection enhances surface convergence by bringing down stronger flows from aloft. The enhanced surface convergence leads to stronger convection, which cools and dries the subcloud layer, and hence increases surface pressure. The system comes to equilibrium when the outward pressure gradient force and surface drag balance the tendency due to the downward momentum advection.

The bottom-heaviness of the eigenmodes of $[L(\cdots)_p]_p$ with $L = \eta\partial/\partial z$ is also manifested in the stronger negative lower-troposphere peak between wavelengths of 6000 and 16 000 km, and a first baroclinic structure that peaks at a lower altitude for wavelengths longer than 16 000 km, compared to the Rayleigh and diffusive momentum damping cases (third and fourth columns in Figs. 10 and 11). In both aspects, results with $L = \eta\partial/\partial z$ are in better agreement with results with the CSRM-derived **L**, indicating again the importance of the downward advection aspect of the CMT.

9. Summary and conclusions

We have investigated behaviors of Walker cells driven by weak SST forcing. The goal is to gain insight into steady tropical circulations through this simple example.

We started with CSRM simulations with planetary-scale domain sizes where both cumulus scale motions and the large-scale Walker circulation are explicitly simulated. We found that for the same ΔSST forcing, the resulting Walker circulation strength is substantially stronger with longer domain sizes, even though the SST gradient is weaker. With the increasing domain size, the vertical velocity profiles also become progressively less top-heavy, with mostly a first baroclinic structure. For planetary-scale domains, the temperature anomalies are dominated by a second baroclinic structure, being colder below about 500 hPa and warmer above, and the cold anomalies are stronger than the warm anomalies, leading to a higher surface pressure over the warmer SST. Near-surface horizontal winds there are nevertheless convergent. As the x-domain size increases, the second baroclinic temperature anomaly slightly strengthens, even though the second baroclinic component in vertical velocity diminishes. Moreover, over the warmer SSTs, air is drier near the surface but moister aloft and becomes more so as the domain size increases.

We then used a simplified system to reproduce the results from the explicit planetary-scale Walker simulations, where we represent the cumulus ensemble with its linear response functions and parameterize the large-scale flow based on the gravity wave equation.

We constructed linear response functions for two cases, one with unorganized convection and the other with strong convective organization. We found that sensitivities of convective heating/moistening to temperature and moisture anomalies depend strongly on convective organization. With unorganized convection, such sensitivities are consistent with a parcel view of convective overturning, where an anomalously warm layer forms a buoyancy barrier that eliminates certain convective updraft parcels, causing cooling at and above the layer, while an anomalously moist layer reduces the degree of entrainment drying experienced by the parcels and allow them to reach higher, causing warming at and above the layer. On the other hand, the sensitivities to temperature and moisture anomalies in the case with strong convective organization are consistent with a layer mode of convective overturning, where convective inflows are much deeper than the subcloud layer, and warm and moist anomalies in the lower troposphere and cold and moist anomalies in the upper troposphere lead to enhanced convective heating throughout the free troposphere.

Convective systems in the explicit Walker simulations show strong organization. When linear response functions of the strong convective organization case are used, our simplified system reproduces quite well results from the explicit Walker simulations. Results with linear response functions of the unorganized-convection case show worse agreement, demonstrating that the differing sensitivities caused by the different degrees of convective organization have significant effects on the resulting Walker circulations. In particular, because with strong convective organization, convective heating in response to temperature and moisture anomalies is predominantly of the same sign throughout the free troposphere, there is a much weaker second baroclinic component in the convective heating anomalies, which limits the second baroclinic component in the vertical velocity profiles of the resulting Walker circulations. We note that the mock Walker cell setup does seem to exaggerate the extent of convective organization (Fig. 2 resembles a gigantic squall line). Convective organization in nature likely falls between those seen in our Walker cells and the 2048-km case and those seen in the unorganized 128-km case.

We then explored the effect of different treatments of the momentum equation on the resulting Walker cells. We advanced an argument, made originally in Kuang (2011), for a mechanism that causes the vertical velocity profiles of the Walker cells to have broader vertical scales at large horizontal domain sizes. As horizontal wavelength increases, the temperature anomaly required to sustain a vertical velocity anomaly of given amplitude increases. Because the sum of the convective tendencies associated with the temperature anomaly and the vertical advection tendencies associated with the vertical velocity anomaly must balance the imposed forcing, the amplitude of vertical velocity will be limited when the ratio of temperature anomaly to the vertical velocity anomaly becomes sufficiently large. Because this ratio is greater for modes with smaller vertical scales, expressed in terms of higher eigenvalues for these modes in Eq. (13), such modes feel this constraint more strongly and modes with broader vertical scales become more dominant as the horizontal wavelength increases.

The relaxation/WTG approach neglects the vertical-scale dependence of the temperature anomalies required to maintain a vertical velocity anomaly and therefore lacks the mechanism to move toward broader vertical scales at long horizontal wavelengths. In contrast, all approaches based on the gravity wave equation capture the tendency toward broader vertical scales as horizontal wavelength increases. Significant differences, however, are seen with different forms of CMT. These differences were understood in terms of the differing

eigenmodes and eigenvalues of the operator on the left-hand side of Eq. (8).

With Rayleigh damping, the rate of increase in the eigenvalues (or the amplitude of the temperature anomaly required to sustain a vertical velocity anomaly of given amplitude) with decreasing vertical scales is relatively modest compared to those with downward momentum advection and diffusive momentum damping (Fig. 16d). Therefore, the tendency toward broader vertical scales is not as strong as in those two cases.

The eigenmodes of $[L(\cdots)_p]_p$ with $L = \eta\partial/\partial z$ are more bottom-heavy than those with Rayleigh and diffusive momentum damping. This bottom-heaviness is expressed as a cold anomaly in the lower troposphere that is stronger than the warm anomaly in the upper troposphere and a higher surface pressure over the warmer SSTs, consistent with results from the explicit Walker cell simulations. Rayleigh and diffusive momentum damping do not capture this behavior. This bottom-heaviness is also manifested in the shape of the vertical velocity profiles, showing generally better agreement with results with the CSRM-derived linear response function for CMT.

The above results indicate that because of its effect on the vertical velocity profile (and hence the GMS) and the subcloud-layer temperature and humidity (and hence surface fluxes), properly accounting for horizontal momentum balance with the gravity wave approach and the downward advection aspect of CMT is important to explaining the counterintuitive results of stronger Walker cells with larger horizontal domains and the high surface pressures over the warmer SST.

The fact that the Walker cell response to the same SST forcing can vary significantly with horizontal wavelength, with the degree of convective organization, and with different forms of CMT, in the absence of any WISHE or radiative feedbacks, shows the richness in the behavior of system. It is hoped that through analyses of this simple example of steady tropical circulation, the present work can inform studies on the more complete system. Our analysis of the effects of different forms of CMT, for example, could inform global climate model studies of such effects on the general circulation (e.g., Bacmeister and Suarez 2002; Wu et al. 2003; Richter and Rasch 2008).

We have neglected rotation in this study. As one moves away from the equator, additional rotational trapping could become important (see, e.g., Blossey et al. 2009). However, the basic argument made here should still apply: with either rotational or convective trapping, the temperature anomalies required to drive a given divergent flow increases with horizontal scale, and eventually becomes significant to affect convection and the overall circulation.

Acknowledgments. The author is grateful to David Neelin and Chris Bretherton for valuable discussions and to Huiqun Wang and Chris Walker and two anonymous reviewers for constructive comments that improved the presentation of this paper. This research was partially supported by NSF Grants ATM-0754332 and AGS-1062016. The Harvard Odyssey cluster provided much of the computing resources for this study.

APPENDIX A

Construction and Test of the Linear Response Functions

We follow Kuang (2010) in the construction of the linear response functions. This appendix describes the specifics of the construction as well as a test of the adequacy of the linear response functions.

In addition to the control experiment, we run a set of sensitivity experiments. In each of the experiments, we include in the model, one at a time, a set of time-invariant, horizontally uniform, anomalous temperature, moisture, or u velocity forcings. The ith ($i = 1, 2, \ldots$) perturbation forcing of each variable takes the form

$$F_i(p_k) = \frac{1}{2}\left\{\delta_{ik} + \exp\left[-\left(\frac{p_k - p_i}{75\,\mathrm{hPa}}\right)^2\right]\right\},$$

where p_k and p_i are the pressure of the kth and the ith model layer, respectively, and δ_{ik} is the Dirac delta function. This form is not optimized and is chosen simply to include both a relatively broad perturbation and a perturbation over the scale of individual model layers. This way, the forcing functions have sizable projections on eigenmodes with broad vertical structures as well as those with more local structures. The moisture portion of the state vector extends to about 200 hPa, above which there is little moisture, while the temperature and u-velocity portion of the state vector extends to above 100 hPa. A height-independent 50-day linear damping is applied to domain-mean temperature, moisture, and u anomalies (departures from their respective reference profiles). This weak damping is applied to limit anomalies in the stratosphere where convective tendencies are too small to balance the applied forcing perturbations.

The amplitudes of the forcings (values to multiply F_i by) are chosen by balancing signal-to-noise ratios, which favor stronger forcing, and linearity, which favors weaker forcing. The amplitudes of the temperature and moisture forcing are 0.5 K day^{-1} and 0.2 g kg^{-1} day^{-1}, respectively, and halved above 10 km (~275 hPa). The amplitude of the momentum forcing at all levels is

0.8 m s^{-1} day^{-1} for the 64-layer 128-km case and 0.4 m s^{-1} day^{-1} for the 28-layer 128-km case. The 2048-km case exhibits greater nonlinearity so we set the amplitude of the momentum forcing to 0.2 m s^{-1} day between 750 and 400 hPa, 0.1 m s^{-1} day^{-1} above 175 hPa, and 0.4 m s^{-1} day^{-1} everywhere else. The degree of linearity is checked by comparing positive and negative forcing runs for temperature and moisture and by comparing with runs with halved forcing amplitudes for u.

When the model reaches a new equilibrium, the anomalous convective tendencies $d\mathbf{x}/dt$ are those that balance the prescribed tendencies and the linear damping. The departure of the new equilibrium T, q, and u from the control experiment provides estimates of $\mathbf{x}$. With this approach, the cumulus ensemble is in statistical equilibrium with the large-scale state as demanded by Eq. (1), and we have neglected the finite response time of convection.

Repeating the calculation for all components of the state vector $\mathbf{x}$ produces a matrix equation

$$\mathbf{Y} = \mathbf{GX}, \tag{A1}$$

where matrix $\mathbf{Y}$ consists of column vectors that are the anomalous convective tendencies and matrix $\mathbf{X}$ consists of column vectors that are estimates of $\mathbf{x}$. The matrix $\mathbf{G}$ can then be computed.

We run the model for 1000 days for the 64-layer 128-km case, 4000 days for the 28-layer 128-km case, and 2000 days for the 2048-km case. The first 100 days are discarded and the rest of the run are averaged to produce columns of $\mathbf{X}$ and $\mathbf{Y}$ in Eq. (A1). For temperature and moisture perturbations, results from positive and negative perturbation runs are combined to improve accuracy. Because of its strong convective organization, the 2048-km case has considerably larger internal fluctuations, which lead to somewhat noisier results than 128-km cases. With this approach, errors are the largest for the fastest-decaying eigenmodes. This can cause some eigenvalues to have a large positive real component (Kuang 2010). Since the CSRM RCE states are evidently stable, we simply reverse the signs of such eigenvalues. The actual decay rates of such eigenmodes are therefore uncertain. However, as they decay very fast, their precise decay rates have little effect on the 4-h average tendencies presented in Fig. 8 and on the coupling with large-scale dynamics.

As a test of the adequacy of the linear response functions as well as an illustration of the difference among the different convective organizations, we take the vertical velocity profile from the 25 000 km × 64 km Walker simulation as shown in Fig. 7 and the surface forcing F_θ and F_q (see section 6 for their calculations), and compute the response in θ', q' from Eq. (10). We also show θ' and q' from a full CRSM simulation forced with the same vertical advection and surface forcings, as well as θ' and q' from such a simulation with the signs of the vertical advection and surface forcings reversed. The signs of θ' and q' from the latter experiment are flipped back for plotting. The difference among the three cases gives an indication of the degree of the nonlinearity in the problem as well as the adequacy of the linear response matrix (or more precisely the inverse of the linear response matrix). The same tests are done for the u velocity. We force the CSRM with the pressure gradient force taken from the 25 000 km × 64 km Walker simulations (shown in Fig. 7) and compare the resulting u' with those computed from the linear response matrix. Figure A1 shows the results for the 64-layer 128-km case (results from the 28-layer case are similar), while Fig. A2 shows the results for the 2048 km × 64 km case. There is general agreement between results using the linear response function and those from the full CSRM calculations, although there appears to be more nonlinearity in the 2048-km case. Another point of note is that the u profiles are quite different between the 28-layer 128-km case (not shown but similar to the 64-layer results) and the 2048-km case, despite their similar local operators as shown in Fig. 9. The reason is elaborated more in appendix B. We have also included in these figures the u-velocity and θ', q' fields from the Walker simulation for comparison. The 2048-km case appears in closer agreement with the Walker simulation results, but some differences remain.

APPENDIX B

Caution on Using Local Approximations of the Linear Response Functions of Momentum for Quantitative Purposes

The instantaneous linear response functions of momentum $\mathbf{L}$ (again with each columns normalized by the mass of the perturbed layer) are dominated by near-diagonal terms (Fig. B1a). The color scale is highly saturated: the maximum absolute value is over 600 m s^{-1} day^{-1} $[\text{m s}^{-1}\ (100\ \text{hPa})^{-1}]^{-1}$. Despite this near-diagonal dominance, we caution the use of a local approximation to $\mathbf{L}$ for quantitative purpose such as a parameterization of CMT. The matrix $\mathbf{L}$ tends to be dominated by the fastest-decaying eigenmodes, while matrix $\mathbf{L}^{-1}$ tends to be dominated by the slowest-decaying modes. The importance of different eigenmodes depends on the time scale of interest. For the large-scale circulations, the slowest-decaying modes are more important. Therefore, the dominance of near-diagonal terms in $\mathbf{L}$ does not necessarily imply that a local approximation is adequate.

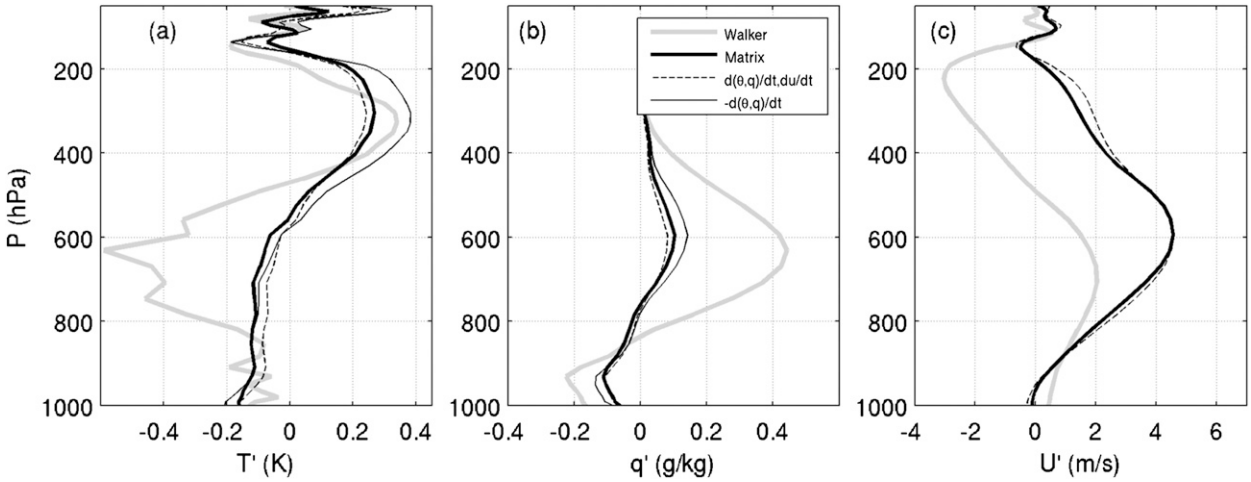

FIG. A1. The steady-state (a) temperature and (b) specific humidity anomalies in response to thermodynamic forcing at the center of the domain from the 25 000 km × 64 km Walker simulation with ΔSST = 0.25°C, and (c) u velocity anomalies in response to pressure gradient forcing at a quarter length of the domain from the same Walker simulation. The thick dark lines are results using the linear response matrix of the 64-layer 128-km case. The thin dashed lines are results from full CSRM simulations (with the same 128 km × 128 km domain and 64 layers). The thin solid lines are also results from full CSRM simulations, but with the sign of the thermodynamic forcing reversed. The sign of the results is flipped back for plotting. Temperature, specific humidity, and u velocity anomalies from the explicit Walker simulation are shown as the gray thick lines.

To illustrate this point, in Fig. B1b we retain the three points centered on the main diagonal, whereas in Fig. B1c we retain the five points centered on the main diagonal. Figures B1d–f show the inverse of the corresponding matrices shown in Figs. B1a–c. While Figs. B1a–c may look similar, the inverses are very different.

Given that $\mathbf{L}^{-1}$ describes the steady-state response to forcing, Fig. B1 shows that despite the dominance of near-diagonal elements in $\mathbf{L}$, a local operator approximation cannot give a quantitative representation of CMT, especially for phenomena with long time scales. The tests described at the end of appendix A provide another illustration of this point. For the Walker cell problem, while not shown here, we have also found that approximating $\mathbf{L}$ with the three points centered on the diagonal captures the qualitative, but not the quantitative, behaviors of the system, with a skill similar to those with $L = \eta\partial/\partial z$ and $L = \kappa\partial^2/\partial z^2$ shown in Figs. 10 and 11.

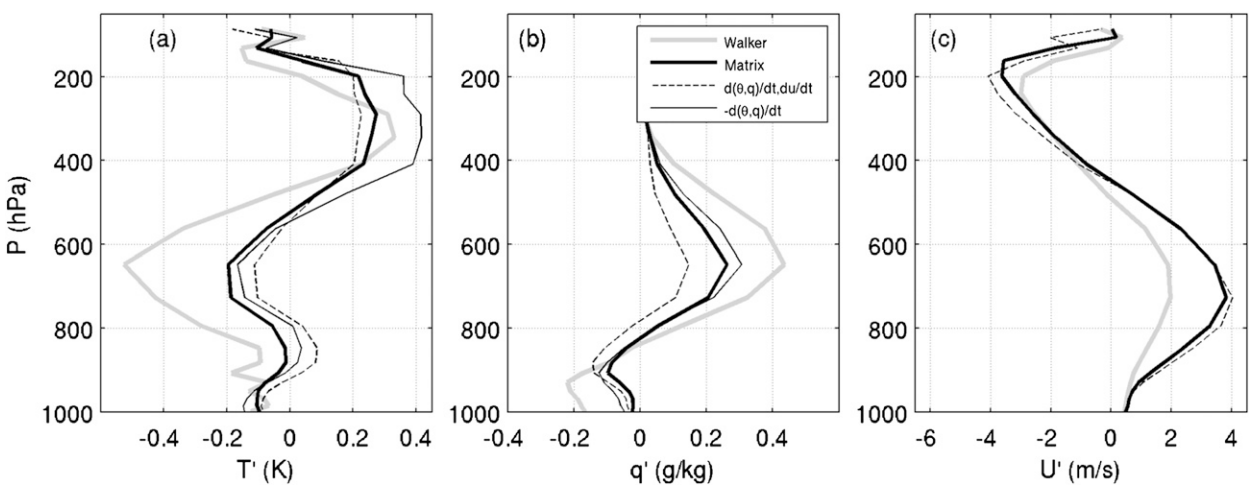

FIG. A2. As in Fig. A1, but for the 2048 km × 64 km limited-domain case. The full CSRM simulations are done with the same 2048 km × 64 km domain and 28 layers. All variables from the explicit Walker simulations, which have 64 vertical layers, are interpolated linearly onto the 28-layer grid of this case.

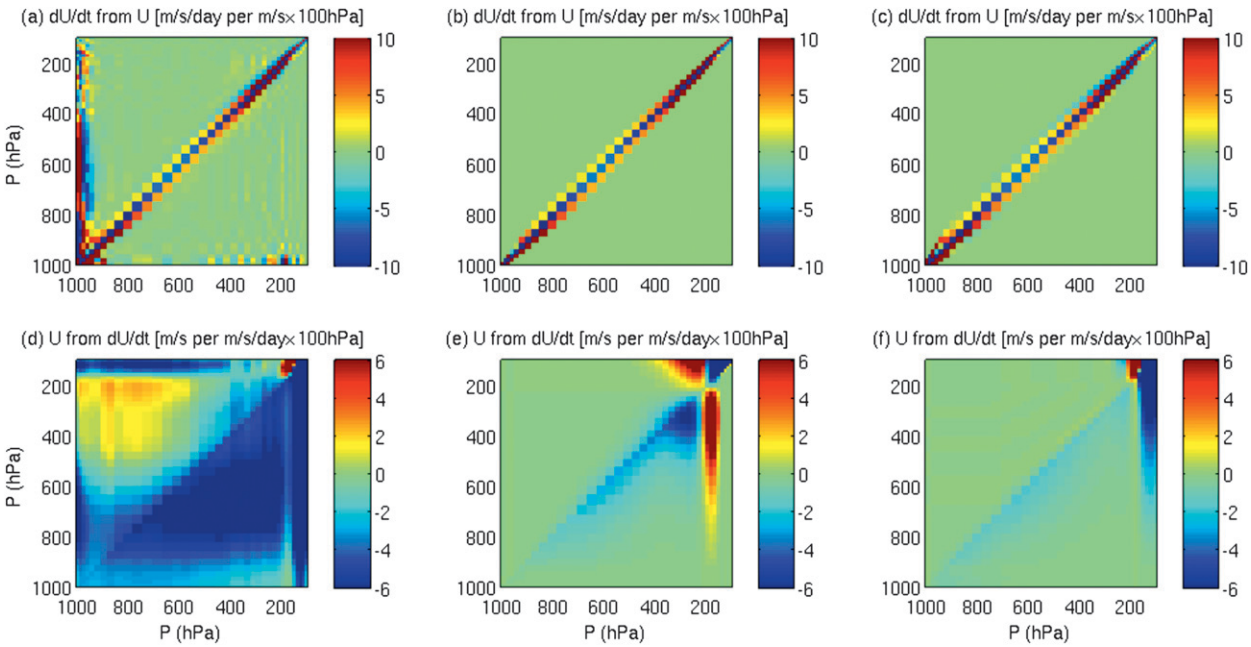

FIG. B1. (a) The **L** matrix of the 64-layer 128-km case, (b) an approximation that retains the three points centered on the main diagonal, and (c) an approximation that retains the five points centered on the main diagonal. (d)–(f) The inverse of the matrices shown in (a)–(c), respectively.

REFERENCES

Bacmeister, J. T., and M. J. Suarez, 2002: Wind stress simulations and the equatorial momentum budget in an AGCM. *J. Atmos. Sci.,* **59,** 3051–3073.

Bergman, J. W., and P. D. Sardeshmukh, 2004: Dynamic stabilization of atmospheric single column models. *J. Climate,* **17,** 1004–1021.

Blossey, P. N., C. Bretherton, and M. C. Wyant, 2009: Understanding subtropical low cloud response to a warmer climate in a superparameterized climate model. Part II. Column modeling with a cloud resolving model. *J. Adv. Model. Earth Syst.,* **1** (8), doi:10.3894/JAMES.2009.1.8.

Bretherton, C. S., P. N. Blossey, and M. E. Peters, 2006: Interpretation of simple and cloud-resolving simulations of moist convection–radiation interaction with a mock-Walker circulation. *Theor. Comput. Fluid Dyn.,* **20,** 421–442.

Brown, R. G., and C. S. Bretherton, 1995: Tropical wave instabilities: Convective interaction with dynamics using the Emanuel convective parameterization. *J. Atmos. Sci.,* **52,** 67–82.

Caldwell, P., and C. S. Bretherton, 2009: Response of a subtropical stratocumulus-capped mixed layer to climate and aerosol changes. *J. Climate,* **22,** 20–38.

Charney, J. G., 1963: A note on large-scale motions in the tropics. *J. Atmos. Sci.,* **20,** 607–609.

Gregory, D., R. Kershaw, and P. M. Inness, 1997: Parametrization of momentum transport by convection. 2. Tests in single-column and general circulation models. *Quart. J. Roy. Meteor. Soc.,* **123,** 1153–1183.

Held, I. M., and A. Y. Hou, 1980: Nonlinear axially symmetric circulations in a nearly inviscid atmosphere. *J. Atmos. Sci.,* **37,** 515–533.

Khairoutdinov, M. F., and D. A. Randall, 2003: Cloud resolving modeling of the ARM summer 1997 IOP: Model formulation, results, uncertainties, and sensitivities. *J. Atmos. Sci.,* **60,** 607–625.

Kingsmill, D. E., and R. A. Houze, 1999: Thermodynamic characteristics of air flowing into and out of precipitating convection over the west Pacific warm pool. *Quart. J. Roy. Meteor. Soc.,* **125,** 1209–1229.

Kuang, Z., 2008: Modeling the interaction between cumulus convection and linear gravity waves using a limited-domain cloud system–resolving model. *J. Atmos. Sci.,* **65,** 576–591.

——, 2010: Linear response functions of a cumulus ensemble to temperature and moisture perturbations and implications for the dynamics of convectively coupled waves. *J. Atmos. Sci.,* **67,** 941–962.

——, 2011: The wavelength dependence of the gross moist stability and the scale selection in the instability of column-integrated moist static energy. *J. Atmos. Sci.,* **68,** 61–74.

LeMone, M. A., 1983: Momentum transport by a line of cumulonimbus. *J. Atmos. Sci.,* **40,** 1815–1834.

Mapes, B. E., 2004: Sensitivities of cumulus-ensemble rainfall in a cloud-resolving model with parameterized large-scale dynamics. *J. Atmos. Sci.,* **61,** 2308–2317.

——, and X. Wu, 2001: Convective eddy momentum tendencies in long cloud-resolving model simulations. *J. Atmos. Sci.,* **58,** 517–526.

Mechem, D. B., R. A. Houze, and S. S. Chen, 2002: Layer inflow into precipitating convection over the western tropical Pacific. *Quart. J. Roy. Meteor. Soc.,* **128,** 1997–2030.

Moncrieff, M. W., 1992: Organized convective systems: Archetypal dynamical models, mass and momentum flux theory, and parametrization. *Quart. J. Roy. Meteor. Soc.,* **118,** 819–850.

Neelin, J. D., and I. M. Held, 1987: Modeling tropical convergence based on the moist static energy budget. *Mon. Wea. Rev.,* **115,** 3–12.

——, and J. Y. Yu, 1994: Modes of tropical variability under convective adjustment and the Madden–Julian oscillation. Part I: Analytical theory. *J. Atmos. Sci.,* **51,** 1876–1894.

Pauluis, O., and S. Garner, 2006: Sensitivity of radiative–convective equilibrium simulations to horizontal resolution. *J. Atmos. Sci.,* **63,** 1910–1923.

Pierrehumbert, R. T., 1995: Thermostats, radiator fins, and the local runaway greenhouse. *J. Atmos. Sci.,* **52,** 1784–1806.

Raymond, D. J., 2007: Testing a cumulus parametrization with a cumulus ensemble model in weak-temperature-gradient mode. *Quart. J. Roy. Meteor. Soc.,* **133,** 1073–1085.

——, and X. P. Zeng, 2005: Modelling tropical atmospheric convection in the context of the weak temperature gradient approximation. *Quart. J. Roy. Meteor. Soc.,* **131,** 1301–1320.

Richter, J. H., and P. J. Rasch, 2008: Effects of convective momentum transport on the atmospheric circulation in the community atmosphere model, version 3. *J. Climate,* **21,** 1487–1499.

Robe, F. R., and K. A. Emanuel, 2001: The effect of vertical wind shear on radiative–convective equilibrium states. *J. Atmos. Sci.,* **58,** 1427–1445.

Schneider, E. K., and R. S. Lindzen, 1976: A discussion of the parameterization of momentum exchange by cumulus convection. *J. Geophys. Res.,* **81,** 3158–3160.

Sessions, S. L., S. Sugaya, D. J. Raymond, and A. H. Sobel, 2010: Multiple equilibria in a cloud-resolving model using the weak temperature gradient approximation. *J. Geophys. Res.,* **115,** D12110, doi:10.1029/2009JD013376.

Shaevitz, D. A., and A. H. Sobel, 2004: Implementing the weak temperature gradient approximation with full vertical structure. *Mon. Wea. Rev.,* **132,** 662–669.

Sobel, A. H., and C. S. Bretherton, 2000: Modeling tropical precipitation in a single column. *J. Climate,* **13,** 4378–4392.

——, G. Bellon, and J. Bacmeister, 2007: Multiple equilibria in a single-column model of the tropical atmosphere. *Geophys. Res. Lett.,* **34,** L22804, doi:10.1029/2007GL031320.

Soong, S. T., and W. K. Tao, 1984: A numerical study of the vertical transport of momentum in a tropical rainband. *J. Atmos. Sci.,* **41,** 1049–1061.

Tulich, S., and B. E. Mapes, 2010: Transient environmental sensitivities of explicitly simulated tropical convection. *J. Atmos. Sci.,* **67,** 923–940.

Tung, W. W., and M. Yanai, 2002a: CMT observed during the TOGA COARE IOP. Part I: General features. *J. Atmos. Sci.,* **59,** 1857–1871.

——, and ——, 2002b: CMT observed during the TOGA COARE IOP. Part II: Case studies. *J. Atmos. Sci.,* **59,** 2535–2549.

Wang, S., and A. H. Sobel, 2011: Response of convection to relative sea surface temperature: Cloud-resolving simulations in two and three dimensions. *J. Geophys. Res.,* **116,** D11119, doi:10.1029/2010JD015347.

Wu, X., and M. Yanai, 1994: Effects of vertical wind shear on the cumulus transport of momentum: Observations and parameterization. *J. Atmos. Sci.,* **51,** 1640–1660.

——, X.-Z. Liang, and G. J. Zhang, 2003: Seasonal migration of ITCZ precipitation across the equator: Why can't GCMs simulate it? *Geophys. Res. Lett.,* **30,** 1824, doi:10.1029/2003GL017198.

Yu, J.-Y., and J. D. Neelin, 1994: Modes of tropical variability under convective adjustment and the Madden–Julian oscillation. Part II: Numerical results. *J. Atmos. Sci.,* **51,** 1895–1914.

Zhang, G. J., and H.-R. Cho, 1991: Parameterization of the vertical transport of momentum by cumulus clouds. Part II: Application. *J. Atmos. Sci.,* **48,** 2448–2457.